



NaNO₃ assisted gelatin-derived multi-level porous carbon aerogel loaded Fe single-atom for high efficient oxygen reduction reaction

Tao Wu^{a,d}, Shufei Zhu^{a,d}, Yiming Xie^{a,*}, Qian Ma^{b,*}, Canzhong Lu^{c,d,**}

^a Engineering Research Center of Environment-Friendly Functional Materials, Ministry of Education, Institute of Materials Physical Chemistry, Huaqiao University, Xiamen 361021, PR China

^b Medical Research Institute, Guangdong Provincial People's Hospital (Guangdong Academy of Medical Sciences), Southern Medical University, Guangzhou 510080, PR China

^c CAS Key Laboratory of Design and Assembly of Functional Nanostructures, and Fujian Provincial Key Laboratory of Nanomaterials, Fujian Institute of Research on the Structure of Matter, Chinese Academy of Sciences, Fuzhou, Fujian 350002, PR China

^d Xiamen Key Laboratory of Rare Earth Photoelectric Functional Materials, Center of Rare-earth Materials, Haixi Institutes, Chinese Academy of Sciences, Xiamen 361021, PR China

ARTICLE INFO

Keywords:

Iron single-atom catalysts
Multi-level pores
Gelatin-derived carbon aerogel
Oxygen reduction reaction
Zinc-air batteries

ABSTRACT

In thrall to the low productivity and expensive price of the precious metal catalysts (PMC), it is imminent to develop high-efficient non-noble metal single-atom catalysts (SACs) to replace PMC. However, thermally induced aggregation into nanoparticles and micropores-dominated structures are commonly encountered issues in loading SACs on carbonaceous supports, leading to low exposure ratio of active sites and inadequate mass transference. Herein, we fabricated a series of gelatin-derived carbon-aerogels (GDCA_x) to prevent the aggregation of Fe atom and form the hierarchically porous nanonetwork, and thus the Fe SACs (Fe-N-GDCA_x) with abundant and hierarchical pores are obtained after pyrolysis. The Fe-N-GDCA_x has plentiful accessible Fe-N_x active sites and mass transfer pathways, benefiting to ORR procedure. The optimal sample Fe-N-GDCA_{0.8} without other gas assisted during annealing (only in argon atmosphere) exhibits exceedingly excellent half-wave potential ($E_{1/2}$) of 0.93 V (vs. RHE) in 0.1 M KOH. Aqueous zinc-air battery assembled with Fe-N-GDCA_{0.8} presents ultrahigh specific capacitance of 803.4 mAh g_{Zn}⁻¹ (close to 824 mAh g_{Zn}⁻¹ theoretical value) and long-term stability. Meanwhile, quasi-solid zinc-air battery has high peak density and specific capacitance of 82.6 mW cm⁻² and 713.2 mAh g_{Zn}⁻¹ respectively.

1. Introduction

To curb the trend of global warming, it is crucial to reduce the consumption of fossil energy and the emission of greenhouse gases. Therefore, the development of advanced high-efficiency clean energy is imminent [1,2]. Zinc-air batteries (ZABs) as a promising alternative to conventional fossil fuels have attracted the interest of countless researchers [3–5]. However, due to the sluggish kinetics of the oxygen reduction reaction (ORR) in cathode and the high dissociation energy of the O=O bond (493.59 KJ mol⁻¹), the development of ZABs is limited [6,7]. Meanwhile, the commonly used ORR cathode catalysts on the market are still dominated by commercial Pt/C, but it has some disadvantages such as low production, expensive price, uneven distribution,

and toxic sensitivity [8–12]. Therefore, exploring effective and efficient noble metal-free catalysts is significant to overcome the shortcomings of noble metal catalysts as well as regulating some harsh problems of the environment.

Among the previously reported M-N-C catalysts, Fe-N-C catalyst possesses the highest oxygen reduction activity in non-noble metal catalysts. However, it is difficult to control the formation of atomically disperse active Fe-N_x sites at high temperature by simply mixing iron source, nitrogen source and carbon source [13–15]. Cause they are prone to agglomeration due to thermal migration during calcination, not only forming inactive Fe nanoparticles but also hindering the electrolyte penetration toward real active sites [16,17]. Therefore, constructing a hierarchical porous nitrogen-doped carbon-supported iron single-atom

* Corresponding authors.

** Corresponding author at: CAS Key Laboratory of Design and Assembly of Functional Nanostructures, and Fujian Provincial Key Laboratory of Nanomaterials, Fujian Institute of Research on the Structure of Matter, Chinese Academy of Sciences, Fuzhou, Fujian 350002, PR China.

E-mail addresses: ymxie@hqu.edu.cn (Y. Xie), maqian@gdph.org.cn (Q. Ma), czlu@fjirsm.ac.cn (C. Lu).

<https://doi.org/10.1016/j.apcatb.2023.122685>

Received 2 November 2022; Received in revised form 24 February 2023; Accepted 22 March 2023

Available online 23 March 2023

0926-3373/© 2023 Elsevier B.V. All rights reserved.

catalyst plays an important role in solving this problem. Abundant open pores can improve the ability of mass transfer and enhance exposure proportion of active sites, making an excellent performance of the Fe-N-C catalyst. Moreover, a high specific surface area can accommodate more active sites, especially the macro/mesopores that are highly exposed on the surface of the catalysts with appropriate micropores which can confine the active Fe-N_x sites [18–21]. So it is challenging but profound to prepare a multi-level porous cross-linked carbon matrix for supporting SACs.

The production of hierarchical porous carbon usually exploits the porous character of the precursor or uses a template method (such as SiO₂) to create pores. But the original pores of precursor are easy to shrink and collapse under high temperature. Furthermore, template methods complicate the preparation process and increase the cost, subsequent removal of the template usually involves acid washing or alkali washing, which is also environmentally unfriendly [22–24]. The use of neutral salts is a promising template method to promote pores engineering, which has the features of convenient movement, environmental friendliness, and low cost [25]. For example, Zhang et al. used NaCl as temple to create meso/micropore-rich electrocatalysts with a high density of accessible Fe-N_x active sites, which had excellent ORR activity [26]. Recently, salt template method has gotten more and more attention [27–29]. The salt template methods can be divided into two active mechanisms, one is physical space occupancy to create pores, and the other is chemical reaction etching. Micropores are usually produced by volatilization after space occupation, such as ZnCl₂, but it is difficult to create abundant mesopores [30]. Therefore, the combination of physical footprint and chemical etching is an efficient method to create a great deal of meso/micropores, even macropores.

Here in, we fabricated a series of SACs (Fe-N-GDCA_x) for efficient ORR by synthesizing hierarchical gelatin-derived carbon-aerogels (denoted as GDCA_x, $x = m_{\text{gelatin}}/m_{\text{NaNO}_3}$) as carbon supports and using iron(II)-phenanthroline complexes (denoted as [Fe(phen)₃]²⁺) as Fe precursors. In this strategy, the gelatin was used as N/O self-doped carbon-aerogel precursor and the NaNO₃ was used as pore-forming agent. To hence the accommodation and isolation of Fe atoms, we deliberately construct abundant micropores and N-doped carbon walls to improve the adsorption of [Fe(phen)₃]²⁺ and space separation of Fe-N_x. Furthermore, there are plentiful macropores and mesopores present in GDCA_x, which can reservoir electrolytes and accelerate the process of mass transfer, respectively. Benefiting from the N/O-doped macro-meso-microporous structure of Fe-N-GDCA_x, Fe atom active sites can be adequately exposed, then superbly improve the ORR activity [31]. Meanwhile, the effect of different dose of NaNO₃ on the ORR performance was also explored, elucidating from the aspects of defect degree, pore structure, N heteroatom species and electrochemical active area of Fe-N-GDCA_x. The optimized Fe-N-GDCA_{0.8} exhibited an ultrahigh half-wave potential ($E_{1/2}$) of 0.93 V in 0.1 M KOH and an attractive specific capacity of 803.4 mAh g_{Zn}⁻¹ (corresponding to ~97.4% of the theoretical value) in aqueous ZABs. Meanwhile, an excellent peak power density of 82.6 mW cm⁻² was achieved in quasi-solid ZABs, indicating that Fe-N-GDCA_{0.8}-based ZABs had potential application advantages in small portable devices.

2. Experimental section

2.1. Catalyst preparation

2.1.1. Synthesis of gelatin derived carbon aerogel (GDCA_x, $x = 0.0, 0.4, 0.8$ and 1.2)

The GDCA_x was synthesized by the following four parts: preparing hydrogel, freeze-drying, annealing, and washing with water. Firstly, 5.0 g gelatin (≥ 99.0%, Macklin) was dissolved in 115 mL ultrapure water (18.25 MΩ·cm) with continuous magnetic stirring under 80 °C until it became a transparent solution. Then 4.0 g NaNO₃ powder (≥ 99.0%, Macklin) was added into the solution with 15 min faster stirring and

placed the solution into the freezer for 30 min to form hydrogel. Second, put the hydrogel into the Dewar basin, froze in liquid nitrogen for 2 min, then place it in – 60 °C lyophilizer for 48 h. After that, the light white aerogel was obtained. Thirdly, the aerogel was annealed in an argon atmosphere under 800 °C for 2 h with a heating rate of 5 °C/min. Finally, the obtained GDCA_{0.8} was washed with a large amount of deionized water for three times and then dried at 80 °C for 8 h. The other GDCA_x was obtained by the same process, except the weight ratio of the NaNO₃ to gelatin was adjusted to 0, 0.4, 1.2.

2.1.2. Synthesis of Fe-N-GDCA_x, Fe-N-ACET and Fe-N-KJB

The [Fe(phen)₃]²⁺ complex was prepared by mixing 3.0 mg of FeCl₂ (≥ 99.5%, Aladdin) and 12.8 mg of 1,10-phenanthroline (≥ 99.0%, Aladdin) in 60 mL ethanol under violently magnetic stirring to form a dark red solution. Then 60 mg of GDCA_x was poured into the solution, ultrasonicated for 50 min and stirred with the rotation speed of 500 rpm for 5 h at 70 °C. The remaining dispersion was then poured into a glass garden and frozen in liquid nitrogen for 3 min. After one day of freeze drying, the obtained black powder was placed in a tube furnace and heated to 800 °C under Ar atmosphere for 2 h. After that, four samples of Fe-N-GDCA_{0.0}, Fe-N-GDCA_{0.4}, Fe-N-GDCA_{0.8}, Fe-N-GDCA_{1.2} were obtained. Fe-N-ACET and Fe-N-KJB were synthesized in the same way. Acetylene carbon black and Ketjenblack were purchased from the fuel cell store.

2.2. Physicochemical characterization

Thermogravimetry-mass spectrometry (TG-MS) and thermogravimetry (TG) data were collected by thermo plus EVO2 and Mettler Telodo TGA/DSC 1 from 30 ° to 800 °C. Field emission scanning electron microscopy (FESEM) images and element energy spectrum were obtained from the Apreo S LoVac at an acceleration voltage of 10 kV and 15 kV respectively. High-resolution transmission electron microscopy (HRTEM) images, selected area electron diffraction and element mapping images were collected by FEI Tecnai G2 F20 at an accelerating voltage of 200 kV. Aberration-corrected high angle annular dark field scanning transmission electron microscopy (AC-HAADF-STEM) images were collected on a JEM-ARM200F operating at 300 kV. Powder XRD patterns were conducted over the 2θ range 5–80° on a Miniflex 600 X-ray diffractometer equipped with a Cu Kα radiation source ($\lambda = 1.54$ Å). Raman spectra were obtained on a Renishaw inVi laser confocal microscopic Raman spectrometer equipped with a 532 nm laser excitation source. N₂ adsorption-desorption isotherms were acquired through Quantachrome Autosorb-iQ apparatus at 77 K. X-ray photoelectron spectroscopy (XPS) data were got on a Thermo Scientific K-Alpha with Al-Kα X-ray source ($h\nu = 1486.7$ eV), the value of charge corrections was calculated from the C1s value set at 284.8 eV. The iron content of the sample was detected by inductively coupled plasma optical emission spectrometry (ICP-OES) on Agilent 5110 (OES). Details of characterizing the solid phase with X-ray absorption fine structure (XAFS) analyses. Fe K-edge analysis was performed with Si (111) crystal monochromators at the BL11B beamlines at the Shanghai Synchrotron Radiation Facility (SSRF) (Shanghai, China). Before the analysis at the beamline, samples were pressed into thin sheets of 1 cm in diameter and sealed using Kapton tape film. The XAFS spectra were recorded at room temperature using a 4-channel Silicon Drift Detector (SDD) Bruker 5040. Fe K-edge extended X-ray absorption fine structure (EXAFS) spectra were recorded. Negligible changes in the line-shape and peak position of Fe K-edge XANES spectra were observed between two scans taken for a specific sample. The XAFS spectra of these standard samples (FePc, Fe foil, FeO, Fe₂O₃) were also recorded. The spectra were processed and analyzed by the software codes Athena and Artemis.

2.3. Electrochemical characterization

Electrochemical characterization was executed on CHI 760E (Chen-

hua, China) electrochemical workstation with a general three electrode system at 25 °C. The three-electrode system consisted of working electrode, reference electrode and counter electrode. The Nernst equation was used to converse potentials from the reference electrode to the RHE scale:

$$E_{RHE} = E_{H_2/H_2O} + 0.0591 \times pH + 0.241 \quad (1)$$

Under 0.1 M KOH testing condition, the working electrode was catalyst loading rotating disk electrode, reference electrode and counter electrode were calibrated saturated calomel electrode (reference electrode was almost no potential difference with a new Hg/Hg₂Cl₂ electrode) and platinum mesh electrode respectively. The uniform catalyst ink was prepared by mixing 5 mg catalyst, 225 μL isopropyl alcohol, 255 μL ultrapure water, 20 μL Nafion (5 wt%, Alfa) together, then ultrasonicated for 1 h. For comparison, commercial Pt/C (20 wt%, Shanghai Hesen) was also tested in RRDE with a loading of 0.4 mg cm⁻².

O₂ or N₂ was successively purged into the electrolytic cell with the flow rate of 65 sccm min⁻¹ for 40 min to ensure that the O₂ or N₂ in the test environment was saturated. For rotating disk electrode tests (RDE, 3 mm in diameter), linear sweep voltammetry (LSV) curves were obtained by testing at 400–2500 rpm in the atmosphere of O₂ and N₂ with the scan rate of 10 mV s⁻¹, respectively. The final LSV curve was obtained by subtracting the nitrogen background current. RDE technique was conducted to measure the kinetic current density (*j_k*) and electron transfer numbers (*n*) in the ORR process, which was calculated from the following Koutecky-Levich equation:

$$\frac{1}{j} = \frac{1}{j_L} + \frac{1}{j_k} = \frac{1}{B\omega^{1/2}} + \frac{1}{j_k} \quad (2)$$

$$B = 0.62nFC_0D_0^{1/2}V^{-1/2} \quad (3)$$

For rotating ring-disk electrode tests (RRDE, 4 mm in diameter), the electron transfer number(*n*) and peroxide (H₂O₂) yield were calculated from the following equals:

$$H_2O_2(\%) = 200 \times \frac{I_r}{I_d + I_r} \quad (4)$$

$$n = \frac{4I_d}{I_d + I_r} \quad (5)$$

Where *I_d* is the disk current, *I_r* is the ring current, *N* = 0.424 is the collection efficiency constant of the ring.

2.4. Aqueous primary Zn-air batteries fabrication and test

The anode of the zinc-air battery was composed of a 0.5 mm thick zinc plate, which had been polished before use. The cathode consisted of Ni foam, waterproof layer and catalyst layer. (The catalyst loading is 1 mg cm⁻²). The catalyst ink was obtained by dispersing 5 mg Fe-N-GDCA_{0.8}, 1 mg carbon black in 200 μL water and 750 μL isopropyl alcohol and ultrasonicated for 20 min firstly. Then dropped 50 μL Nafion into uniform ink and continuously sonicated for 1 h. To compare, commercial 20% Pt/C catalyst ink was also prepared in the same way. The electrolyte of the Zn-air battery was prepared by mixing 0.2 M Zn (Ac)₂ (≥ 99.9%, Macklin) and 6 M KOH. The OCP was tested by universal meter and open circuit potential-time (OCPT) technique. The polarization curve and the galvanostatic discharge test were carried out by using CHI 760E workstation at room temperature.

2.5. Quasi-solid Zn-air batteries fabrication and test

Quasi-solid Zn-air batteries consisted of a zinc foil (thickness 0.08 mm), gel polymer electrolyte and a carbon cloth loading 1 mg cm⁻² Fe-N-GDCA_{0.8} electrocatalyst. Zinc foil was polished until smooth before using. The carbon cloth was treated with PTFE (60 wt%,

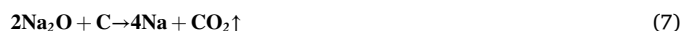
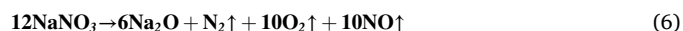
Alfa) to prevent diffusion during casting catalyst ink. The solid electrolyte was prepared by the following steps: Firstly, adding 5 g polyvinyl alcohol (≥ 99.0%, Macklin) into 45 mL deionized water at 95 °C under violently stirring until it became homogeneous solution. Next, 5 mL of 18 M KOH containing 0.2 M Zn(Ac)₂ was injected into the solution. Then keep stirring for 40 min. Finally, the gel solution was transferred in a rectangular mold and stored in the refrigerator at -20 °C for fabricating quasi-solid Zn-air batteries in the future.

3. Result and discussion

3.1. Physical characterizations

The design process of GDCA_x and Fe-N-GDCA_x was shown in Scheme 1 in a cost-effectively and environmentally friendly salt-template way. GDCA_x was synthesized by direct pyrolysis of gelatin-based aerogels containing uniformly dispersed NaNO₃. Gelatin sponge, an N, O-rich macromolecule hydrophilic colloid was chosen as the carbon source, because it can dissolve in hot water and easily form a cross-linked sol-gel network by intermolecular or intramolecular hydrogen bonding effect (Fig. S1) when it cooled down to room temperature [32–34]. Due to the cross-linked network of hydrogels, the aerogel network formed after lyophilization can entangle and accommodate some recrystallized NaNO₃, so that the activators NaNO₃ can encapsulate in the aerogel framework, evidenced by observed crystal-like particles and detected high contained sodium element through SEM and EDS (Fig. S2). When the pyrolysis temperature was raised to 600 °C, NaNO₃ began to decompose and its decomposition products reacted with carbonized gelatin at high temperatures under Ar atmosphere [32,35]. As consequence, the decomposed product Na₂O etched carbon and expanded the size of the pore to form cross-linked hierarchical porous carbon.

In order to obtain highly dispersed and highly exposed active site catalysts, wet-chemical impregnation and freeze-drying assisted approaches were applied to the synthesis of Fe-N-GDCA_x. Firstly, Fe [(phen)₃]²⁺ complex was dispersed in ethanol and water and absorbed by GDCA_x. Then freeze-drying was used to evenly distribute the Fe [(phen)₃]²⁺ complex on the carbon matrix and maintain the pores structure of the carbon matrix. The porous structure separated the iron-containing compounds in space, while the nitrogen on the phenanthroline anchored the iron atoms like tweezers. Subsequently, the Fe-N-GDCA_x catalyst was obtained after high-temperature annealing. In order to observe the surface morphology and microstructure of the material, SEM and TEM were chosen as the characterization methods. SEM images of Fe-N-GDCA_{0.8} in Fig. 1a, b showed a honey-comb-like three-dimensional structure with abundant cross-linked submicron level macropores, which was also confirmed by HRTEM images in Fig. 1c, d. In addition, no Fe nanoparticles or nanoclusters were observed, which preliminarily proved that iron may atomically disperse on the carbon support [36–38]. For comparison, the images of Fe-N-GDCA_{0.0}, Fe-N-GDCA_{0.4}, Fe-N-GDCA_{1.2} were displayed in Figs. S3a-i. Fe-N-GDCA_{0.0} almost had little pores in SEM images, Fe-N-GDCA_{0.4} had some individual macropores on the surface instead of cross-linked continuous macropores, and Fe-N-GDCA_{1.2} showed collapsed holes because Na₂O violently etched the carbon framework and overly broken the cross-linked interpenetrating macro-porous network. This suggests that the appropriate amount of NaNO₃ played an important role in the construction of cross-linked hierarchical porous gelatin-derived Fe-N-C single-atom catalysts. The pore-forming mechanism can be analyzed by TG-MS in (Figs. S4a and S4b) and explained with the following chemical equation:





Scheme 1. Synthesis procession of GDCA_x and Fe-N-GDCA_x.

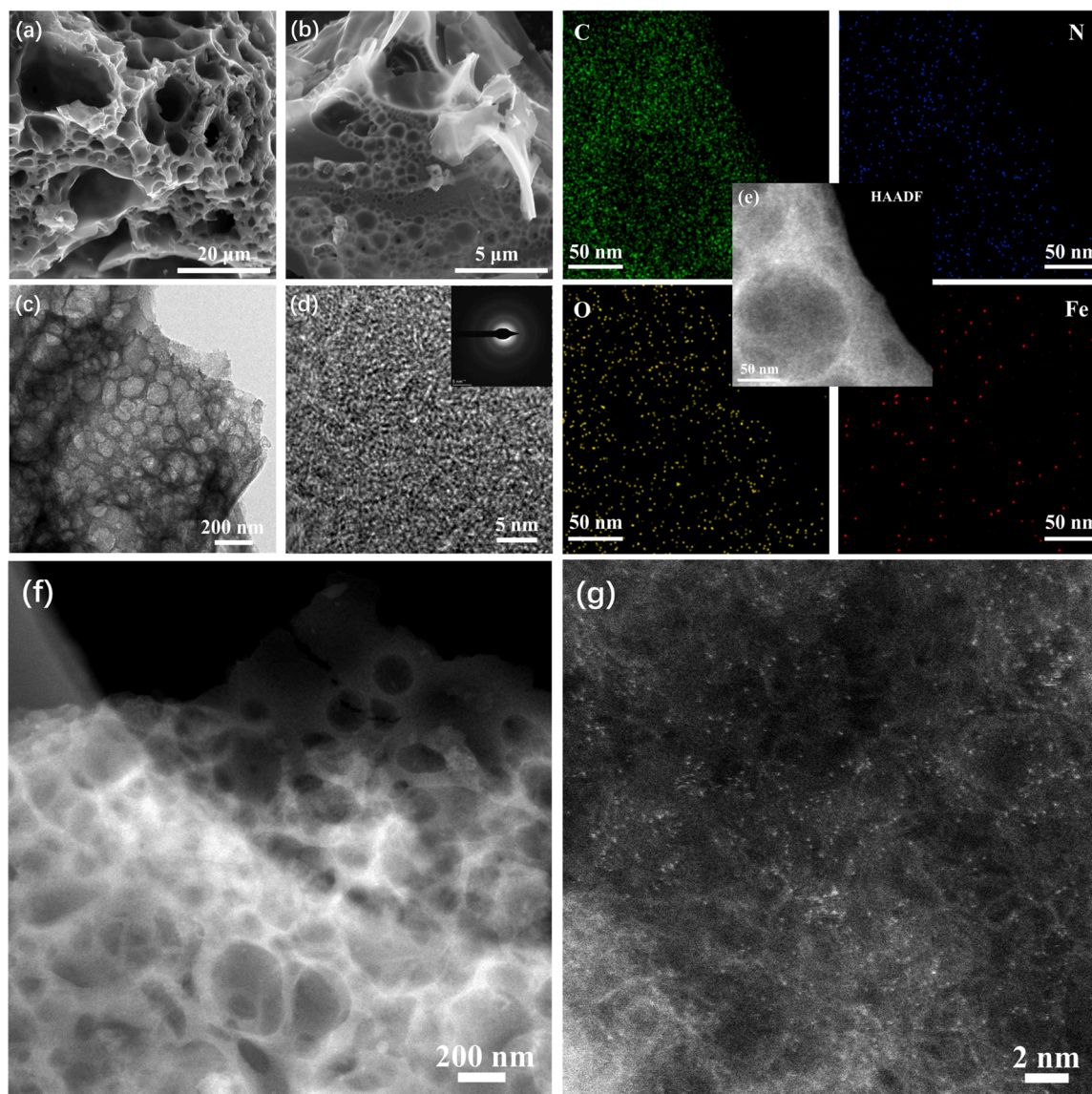


Fig. 1. (a) Low and (b) high-magnification SEM images of Fe-N-GDCA_{0.8}. (c) Low and (d) high-magnification (inset plot: SAED pattern) TEM images of Fe-N-GDCA_{0.8}. (e) The dark-field STEM image and the corresponding EDS elemental maps of Fe-N-GDCA_{0.8}. (f) Dark-field STEM image of Fe-N-GDCA_{0.8}. (g) Aberration-corrected HAADF-STEM image of Fe-N-GDCA_{0.8}.

Firstly, the space occupation effect of NaNO₃ crystal could easily form macropores. Then with the increment of the temperature, the reaction of Na₂O and C could in-situ generate plenty of micropores. Subsequently, the release of CO₂ could both physically and chemically expand the micropores to mesopores. On the one hand, the CO₂ could continuously etch carbon support. On the other hand, the released CO₂ and other gases could enlarge the pores during expanding and escaping [39–41]. The dark field image of HRTEM revealed the foam-like

structure of Fe-N-GDCA_{0.8} (Fig. 1f). Plenty of macropores and mesopores could also be easily observed through HRTEM, indicating the existence of quite a lot of edges and defects, which benefited to the catalyst activity [42–46]. In addition, lattice fringes with a lattice spacing of 0.34–0.42 nm were caught (Fig. S5) and corresponded to the (002) facet of graphite. The slightly increased lattice spacing may be attributed to the expansion and escape of gas during high temperature. The result was agreed with the image of selected area electron diffraction (SAED)

shown in Fig. 1d, revealing no iron-based nanoparticles or nanoclusters in Fe-N-GDCA_{0.8} [47]. Element mappings were employed to reveal the catalyst element distribution in Fig. 1e, with both N, O and Fe elements evenly scattered on the carbon substrate. What was mentioned above all indicated that iron element most likely dispersed on GDCA_{0.8} in the form of single-atom. In order to catch the atomic phase of iron, spherical aberration-corrected high-angle annular dark-field scanning transmission electron microscopy (HAADF-STEM) was applied. As shown in Fig. 1g, ample bright isolated dots stochastically distributed on the porous carbon meant that the iron element was great likely to exist in the form of single-atom.

To deeper understand the phase composition of Fe-N-GDCA_x materials, the powder XRD analysis was employed to explore the catalyst constitution. In Fig. 2a, the samples from NaNO₃ activated GDCA_x ($x = 0.4, 0.8$, and 1.2) displayed a peak around 22°, which was attributed to the characteristic peak of C (002) facet [48,49]. By contrast, Fe-N-GDCA_{0.0} exhibited another sharp diffraction peak on 45°, corresponding to the FeC (JCPDS #06-0686), as shown in Fig. S6. Furthermore, rufous aggregations appeared in unannealed Fe-N-GDCA_{0.0} but were absent in Fe-N-GDCA_{0.8} (Fig. S7). These phenomena demonstrated that gelatin-derived carbon without NaNO₃ had no enough pores to disperse and accommodate the iron organic complex so that the iron compounds agglomerated due to thermal migration under high temperature synthesis conditions [50,51]. Additionally, all Fe-N-GDCA_x samples activated by NaNO₃ were similar to the XRD spectra of its own GDCA_x (Fig. S8), which represented no formation of highly crystalline iron or iron-based complexes during high temperature calcination. Moreover, Raman spectra were used to determine the graphitization degree and structuration defect of materials [52,53]. The intensity of D band (1350 cm⁻¹) and G band (1590 cm⁻¹) showed different graphitization of Fe-N-GDCA_x. As shown in Fig. 2b, the value of I_D/I_G raises up with the increased dose of NaNO₃, which indicates that NaNO₃ may function as pore engineer and increase the defection of catalyst materials. But when the weight ratio of NaNO₃ to gelatin was increased to 1.2, the I_D/I_G value had a little decrease. It may attribute to excessive NaNO₃ could severely destroy the local structuration of the defect which had already formed. So the Fe-N-GDCA_{0.8} has the highest value of I_D/I_G and was beneficial to the ORR process [54].

The nitrogen physical adsorption/desorption test was used to explore

the different doses of NaNO₃ effect on the catalyst porosities, especially the surface area and pore size distribution. The porous properties of the Fe-N-GDCA_{0.0}, Fe-N-GDCA_{0.4}, Fe-N-GDCA_{0.8}, Fe-N-GDCA_{1.2} were shown in Fig. 2c, d. Without using NaNO₃, Fe-N-GDCA_{0.0} only possessed a specific surface area of 44.1 m² g⁻¹. While Fe-N-GDCA_{0.4}, Fe-N-GDCA_{0.8}, Fe-N-GDCA_{1.2} showed a specific surface area of 960.9 m² g⁻¹, 1905.2 m² g⁻¹, 1912.8 m² g⁻¹ respectively. Meanwhile, Fe-N-GDCA_{0.4}, Fe-N-GDCA_{0.8}, Fe-N-GDCA_{1.2} all showed a sharply increasing adsorption/desorption curve at relatively low nitrogen pressure ($P/P_0 = 0-0.01$) and a hysteresis loop was observed at relatively high nitrogen pressure ($P/P_0 = 0.40-0.97$), indicating that coexistence of micropores and mesopores [55-57]. In addition, the GDCA_{0.8} showed a larger specific surface of 2448.5 m² g⁻¹ (Fig. S9) and it significantly became a smaller value of 1905.2 m² g⁻¹ after absorbing metal organic compounds, which also indicated the Fe[(phen)₃]²⁺ complex successfully doped into GDCA_{0.8}. The pore size distribution plots were also used to analyze the pore structure of materials, it showed that Fe-N-GDCA_{0.4} with abundant micropores ranging from 0.5-0.6 nm while only some mesopores ranging from 2.0 to 3.5 nm. With the increment of NaNO₃, both Fe-N-GDCA_{0.8} and Fe-N-GDCA_{1.2} possessed more mesopores ranging from 2.5 to 6.0 nm and larger micropores ranging from 0.7 to 1.2 nm rather than Fe-N-GDCA_{0.4}, which meant NaNO₃ can enlarge the pore sizes and emerge more mesopores.

X-ray photoelectron spectroscopy (XPS) was carried out to analyze the type and state of the surface chemistry elements (Fig. S11). As shown in Fig. 2e, the high-resolution N 1s spectra displayed five different N species characteristic peaks: pyridinic N, Fe-N_x, pyrrolic N, graphitic N and oxidized N [58-60]. With the increasing amount of NaNO₃, oxidized N content decreased gradually. Notably, compared to Fe-N-GDCA_{0.0}, the etching effect of NaNO₃ can create more defects and pores on carbon matrix of Fe-N-GDCA_{0.8}, leading to the high exposure ratio of graphitic N and pyridinic N, and Fe-N-GDCA_{0.8} had the moderate content of graphitic N and pyridinic N near the carbon defective edge, which was confirmed to be a benefit to the ORR process [61-64]. The content of O element decreased from 16.29 at% (Fe-N-GDCA_{0.0}) to 4.10 at% (Fe-N-GDCA_{0.8}), then raised to 4.26 at% (Fe-N-GDCA_{1.2}) as the increasing amount of NaNO₃. This may attribute to appropriate NaNO₃ can etch less stable O-containing species when it decomposed. But using excessive NaNO₃ may lead to rising O content because it may also

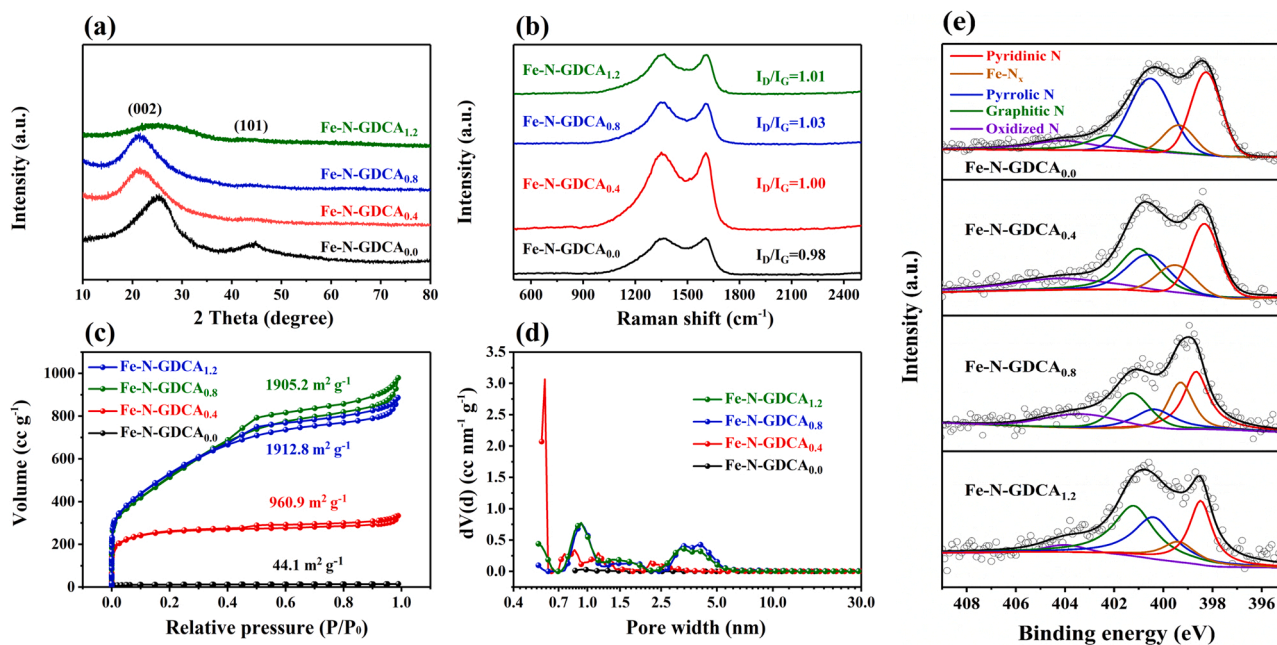


Fig. 2. (a) XRD patterns and (b) Raman spectra for Fe-N-GDCA_x. (c) N₂ adsorption/desorption isotherms and (d) pore size distribution curves for Fe-N-GDCA_x. (e) High-resolution N 1s XPS spectrum for Fe-N-GDCA_x (Fe-N-GDCA_{0.0}, Fe-N-GDCA_{0.4}, Fe-N-GDCA_{0.8}, and Fe-N-GDCA_{1.2}).

produce more O_2 after breaking down. The high-resolution C 1 s spectra (Figs. S12 a-d) were used to explore the defect degree of the four samples, the spectra can be deconvoluted into five types of C species: C-C (sp^2), C-C (sp^3), C=N/C=O, C-N/C=O and shakeup $\pi-\pi^*$ satellite respectively. It is well-known that there are two kinds of carbon atoms in graphene (i.e., the basal-plane sp^2 carbon atoms and the defect sp^3 carbon atoms) [65,66]. So the ratio of C-C (sp^2)/C-C (sp^3) can reflect the defect degree of graphene. The sp^2/sp^3 ratio values of four samples were calculated to be 2.12, 0.87, 0.25 and 0.41 respectively from Fe-N-GDCA_{0.0} to Fe-N-GDCA_{1.2}. The Fe-N-GDCA_{0.8} showed the lowest value, which confirmed it has more defects and was consistent with the result of Raman spectrum. To judge the oxidation states of superficial iron element, the high-resolution Fe 2p XPS spectrum (Fig. S13) was used to analyze the chemical valence of iron. The spectrum exhibited two contributions, which were assigned to Fe^{2+} and Fe^{3+} species. The Fe^{2+} 2p_{3/2} peak was situated at 709.7 eV and the Fe^{3+} 2p_{3/2} peak was located at 711.7 eV, suggesting that the iron in Fe-N-GDCA_{0.8} had two kinds of ionic $Fe^{\delta+}$ ($\delta = +2$ and $+3$). Meanwhile, no zero-valence metallic Fe (706.5 eV) was detected in Fe-N-GDCA_{0.8} further confirming that iron element may exist in the form of single-atom, which was consistent with the previous results of XRD and HAADF-STEM [67]. The iron content (2.54 wt%) of Fe-N-GDCA_{0.8} was detected by inductively coupled plasma optical emission spectrometry (ICP-OES).

In order to deeper understand the valence information and configuration environment of the Fe-N-GDCA_{0.8}, synchrotron-radiation-based X-ray absorption fine structure (XAFS) was used. The Fe K-edge X-ray absorption near-edge structure (XANES) spectrum (Fig. 3a) implied the valence state of the iron single atom located approximately at $+2-3$, which was consistent with the results of XPS [68–70]. The absorption edge of Fe-N-GDCA_{0.8} shifted to higher energy relative to divalent FePc (Fig. S14), also indicating Fe-N-GDCA_{0.8} might possess a higher valence state. According to Fourier-transformed (FT) k^2 -weighted extend X adsorption fine structure (EXAFS) spectrum (Fig. 3b), Fe-N-GDCA_{0.8} was observed a strong signal at around 1.5 Å, which can boil down to the first shell scattering path of Fe-N [71]. The inexistence of a strong signal of the first shell scattering path of Fe-Fe further confirmed that no

agglomerated iron particles in the Fe-N-GDCA_{0.8} electrocatalyst and in agreement with the outcome of AC-HAADF-STEM. Wavelet transformed (WT) EXAFS is also an intuitive way to distinguish Fe-Fe bond and Fe-N bond. The contour plot of Fe foil showed a maximum intensity at 7.3 Å⁻¹ (Fig. 3d), which can be ascribed to the scattering path of Fe-Fe first coordination shell. Fe-N-GDCA_{0.8} contour plot displayed the maximum signal at ca. 3.41 Å⁻¹ (Fig. 3f) and was close to the plot of FePc (ca. 3.42 Å⁻¹ Fig. 3e), which can come down to the Fe-N first shell coordination [72]. Moreover, the fitting results (Fig. 3c, Fig. S15 and Table S1) of FT k^3 -weighted EXAFS spectrum reveal the coordination environment of Fe-N-GDCA_{0.8}. The single atom iron anchored by nitrogen in the electrocatalyst possessed a shorter bond length than Fe foil and a four nitrogen-coordinated structure, which were the real activity sites of the Fe-N-GDCA_{0.8}.

According to above investigations, the as-prepared GDCA_x plays an important role in the formation of hierarchical porous carbon aerogel loaded Fe single-atom. In order to gain a deeper understanding of the GDCA_x structure effect on the formation of Fe-N-GDCA_x, commercial Acetylene carbon black and Ketjenblack (denoted as ACET and KJB, respectively) were taken to compare. According to results of element analysis and isotherms, GDCA_{0.8} showed more self-doping heteroatoms than ACET and KJB as well as possessed a larger specific surface area, a wider pore size distribution (Figs. S9–10 and Table S2). The larger specific surface area and pore volume can accommodate more Fe [(phen)₃]²⁺ complexes. Furthermore, XPS (Fig. S16) were also used to analyze the binding energy of carbonized samples (i.e., Fe-N-ACET, Fe-N-KJB, and Fe-N-GDCA_{0.8}) and their precursor which adsorbed metal-organic complexes (i.e., Fe-Phen@ACET, Fe-Phen@KJB, and Fe-Phen@GDCA_{0.8}). Compared to GDCA_{0.8}, Fe-Phen@GDCA_{0.8} showed a higher binding energy of different N species and a new peak of Fe-N. Meanwhile, the pyridinic N of Fe-Phen@GDCA_{0.8} showed slightly higher binding energy in comparison to Fe-Phen@ACET and Fe-Phen@KJB, and the binding energy of other N species on Fe-Phen@GDCA_{0.8} were positive shift compared to GDCA_{0.8}, indicating that original N species on GDCA_{0.8} may have some affinity to Fe [(phen)₃]²⁺ complexes. For the carbonized samples, the binding energy

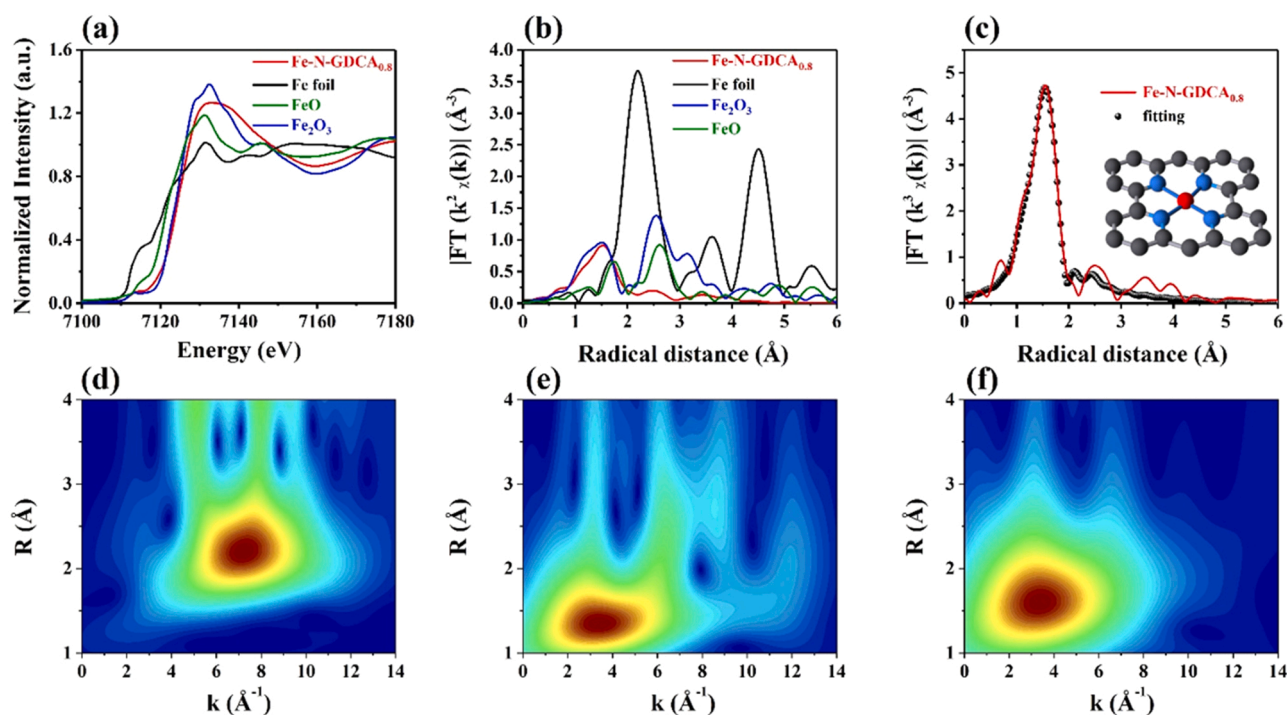


Fig. 3. (a) Normalized Fe K-edge XANES spectra and (b) Fourier-transformed k^2 -weighted EXAFS spectra for Fe-N-GDCA_{0.8} and reference samples. (c) EXAFS R-space fitting curve for Fe-N-GDCA_{0.8}. (d) wavelet transforms for the k^2 -weighted Fe K-edge EXAFS signals for Fe foil. (e) FePc. (f) Fe-N-GDCA_{0.8}.

of each N species showed a negative shift compared with their precursor samples. This may attribute to the formation of bond between iron and nitrogen, the distance between iron and nitrogen atoms became short, and the density of the electron cloud increased, adding the shielding effect of nuclear charge [73–76]. It can be demonstrated that the GDCA_{0.8} matrix not only adsorbed Fe[(phen)₃]²⁺ complexes through pores, but also anchor them by rich heteroatoms. In addition, to compare the influence of carbon matrix on the formation of FeN_x, XRD was carried out to detect the original three carbon matrixes and Fe-loading carbonized catalysts, ICP was used to judge the difference of the iron content among the three samples. Fe-N-ETB (Fe content: 1.14 wt%) appeared a slightly sharp peak around 45°, which indicated

that the generation of Fe nanoparticle, but Fe-N-GDCA_{0.8} (Fe content: 2.54 wt%) and Fe-N-KJB (Fe content: 1.55 wt%) showed no obvious sharp diffraction peak (Figs. S17a-b). The lower iron content of Fe-N-ETB but formation of Fe nanoparticle, which may attribute to the less abundant pore structure and smaller specific surface of ETB (288.4 m² g⁻¹) than GDCA_{0.8} (2448.5 m² g⁻¹) and KJB (1272.4 m² g⁻¹) [77]. By the way, due to the rich micropores and mesopores, KJB can reach a high BET surface area but lack of self-doped N to accelerate the transfer of electron and anchor the iron complexes, so both the $E_{1/2}$ and Fe content of Fe-N-KJB are inferior to Fe-N-GDCA_{0.8}. Therefore, GDCA_{0.8} presented better confinement of Fe[(phen)₃]²⁺ complexes than ACET and KJB, and thus inhibited the intense thermal movement of the

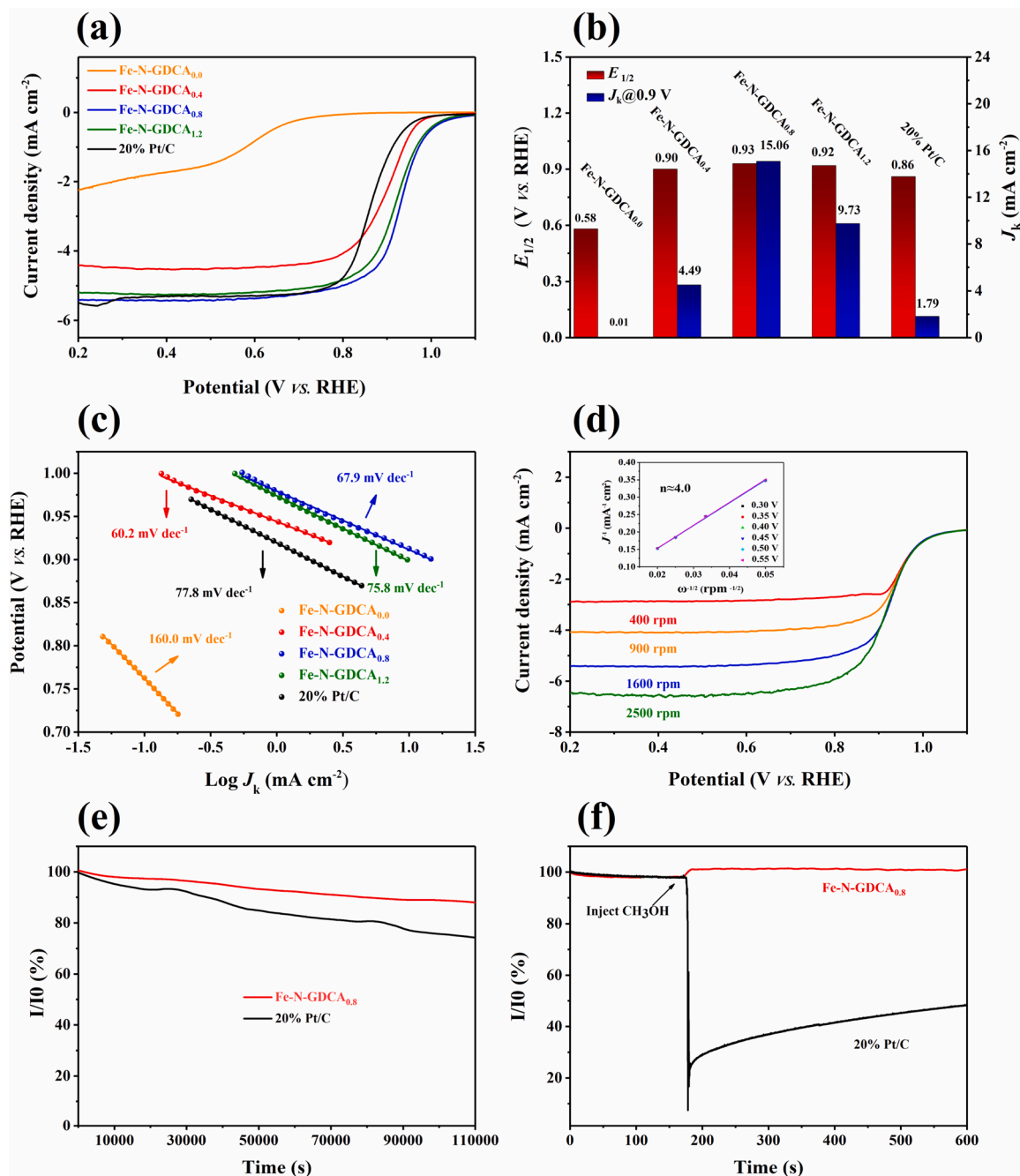


Fig. 4. (a) LSV curves for Fe-N-GDCA_x and Pt/C in O₂-saturated 0.1 M KOH with a rotating rate of 1600 rpm after 95% iR correction. (b) comparison of $E_{1/2}$ and j_k at 0.90 V for different electrocatalysts in O₂-saturated 0.1 M KOH. (c) Tafel plots and (d) LSV curves of Fe-N-GDCA_{0.8} in O₂-saturated 0.1 M KOH with various rotating rates after 95% iR correction. (e) Normalized i-t curves of Fe-N-GDCA_{0.8} and Pt/C at 1600 rpm. (f) Normalized i-t curves of Fe-N-GDCA_{0.8} and Pt/C at 1600 rpm with 3 M methanol addition around 180 s.

complexes under high temperatures. Taking advantages of abundant self-doped N/O atoms and hierarchical porous structure, GDCA_{0.8} displayed superiority in loading Fe single-atoms.

3.2. Electrochemical performance evaluation

The ORR activity of the Fe-N-GDCA_{0.0}, Fe-N-GDCA_{0.4}, Fe-N-GDCA_{0.8}, Fe-N-GDCA_{1.2} and commercial Pt/C (20% Pt, Hesen) catalysts were revealed by linear sweep voltammetry under oxygen-saturated 0.1 M KOH. All potentials had been converted relative to RHE. As seen in Fig. 4a, Fe-N-GDCA_{0.8} possessed more excellent performance than Fe-N-GDCA_{0.4} and Fe-N-GDCA_{1.2} in alkaline conditions. By comparing their LSV curves, Fe-N-GDCA_{0.8} exhibited more positive $E_{1/2}$ (0.93 V) than Fe-N-GDCA_{0.4} (0.90 V) and Fe-N-GDCA_{1.2} (0.92 V), while Fe-N-GDCA_{0.0} only had the $E_{1/2}$ of 0.58 V in the same measure circumstance. Combined with the former structure investigations, it can draw a preliminary conclusion that appropriate NaNO₃ as a pore engineer can create macro-meso-micro multi-level pores, which can increase the exposure ratio of active sites and improve the mass transfer ability of the catalyst. Without NaNO₃ template, gelatin-derived carbon aerogel exhibited extremely low ORR catalytic activity. According to the N₂ adsorption/desorption isotherms-based pore analysis and XRD results, it can be observed that GDCA_{0.0} had few pores to accommodate iron complex and led to the generation of inactive nanoparticles under high temperature. Moreover, the $E_{1/2}$ of Fe-N-GDCA_{0.8} showed 70 mV higher than commercial 20% Pt/C ($E_{1/2}$ = 0.86 V), indicating that Fe-N-GDCA_{0.8} was considerably more active in ORR (Table S3). When it comes to onset potential (E_{onset}) and diffusion-limiting current density (J_L), the Fe-N-GDCA_{0.8} showed the most positive onset potential and the largest diffusion current density, which was measured to be 1.04 V and 5.4 mA cm⁻² respectively. More details compared to other samples were listed in Fig. 4b, Fe-N-GDCA_{0.8} was outperforming other specimens in both J_k and $E_{1/2}$, due to the abundant macro-meso-micro cross-linked porous structuration and highly exposed active sites at the three-phase interface, which were benefited for oxygen access and attach active sites before reaction as well as product diffuse and transfer after reaction [78–80]. In addition, the kinetic current density at 0.9 V (J_k @ 0.9 V) was carried out to compare the activity of different samples, the J_k of Fe-N-GDCA_{0.8} exhibited 15.06 mA cm⁻² at 0.9 V while commercial 20% Pt/C only had 1.79 mA cm⁻² at the same potential, the former was almost 8 times higher than latter. To further explore the activity of the samples for ORR, the Tafel slope derived from LSV was used to judge the reaction kinetics. As shown in Fig. 4c, the slope was determined to be 67.9 mV dec⁻¹ for Fe-N-GDCA_{0.8}, which was quite lower than 77.8 mV dec⁻¹ for Pt/C. The lower Tafel slope, the faster ORR kinetics, indicating that when kinetic current density changed tenfold, it produced a considerably lower overpotential [81–83]. However, Fe-N-GDCA_{0.4} showed the lowest Tafel slope but inferior $E_{1/2}$, it may attribute that the $E_{1/2}$ was controlled by both kinetics and mass transfer diffusion at the same time. Fe-N-GDCA_{0.8} possessed more hierarchical pores and larger specific surface area, so it had greater mass transfer ability than Fe-N-GDCA_{0.4}, leading to the higher $E_{1/2}$. In order to fit out the key reaction kinetic parameters in alkaline condition - electron transfer number, the electrochemical performance test of ORR often uses the rotating disk electrode (RDE) technique under different rotating speeds based on the Koutecký–Levich (K-L) equation to measure the electron transfer numbers about the reaction. The inset about Fe-N-GDCA_{0.8} in Fig. 4d showed a linear relationship between ω^{-1} and j^{-1} at different applied potential ranges 0.30–0.55 V, which conformed to the K-L equation. And the electron transfer numbers were calculated to be approximately approached 4, evidencing a 4 e^{-} transfer oxygen reduction process was preferred to occur in Fe-N-GDCA_{0.8}. Because the RDE method was susceptible to test factors and the parameters were easily changed under different conditions [84,85]. Aimed to obtain an accurate reaction process of the ORR, the rotating ring-disk electrode (RRDE) method was also applied to

determine the electron transfer numbers and H₂O₂ yield. At relatively high potential from 0.6 to 0.9 V, Fe-N-GDCA_{0.8} showed a lower H₂O₂ yield below 2% compared to Pt/C (above 2%). Even at a relatively low potential range from 0.2 to 0.6 V, the H₂O₂ yield of Fe-N-GDCA_{0.8} and Pt/C were both below 5%. Combined with the calculated electron transfer numbers were reach 3.90–3.98, which further proved the efficient four-electron process of O₂ reduction toward OH⁻ (Fig. S18).

Additionally, electrochemical surface area (ECSA) was considered to have a positive linear relationship with double layer capacitance (C_{dl}) [86,87]. In order to determine the effect of different NaNO₃ amounts on ECSA of catalysts, we applied CV technique with various scan rates in non-Faraday region to clarify the C_{dl} of four control samples. Fe-N-GDCA_{0.8} had the highest C_{dl} , which indicated it can provide larger ECSA (Figs. S19 a-d and S20).

The long-time catalytic stability and anti-toxicity are important key indicators to evaluate the performance of ORR catalysts. According to Figs. S21 and S22, 5000 cycles accelerate durability test was applied cyclic voltammetry (CV) technology scan between 0.6 and 1.0 V at 50 mV s⁻¹ scan rate. After testing, $E_{1/2}$ of Fe-N-GDCA_{0.8} only attenuated 20 mV and the current density still retained 92% of the initial J_L , while $E_{1/2}$ of 20% Pt/C decayed 50 mV and its limiting-diffusion current density only kept 79% of the original J_L , which illustrated Fe-N-GDCA_{0.8} had excellent working stability compared to commercial Pt/C. Meanwhile, we also introduced i-t chronoamperometry (CA) tests to monitor the current change while the catalysts working (Fig. 4e). The Fe-N-GDCA_{0.8} retained 87% of the original current density while the Pt/C only retained 74% of the initial current density. Moreover, i-t technology was also carried out to test the anti-methanol poisoning of the catalysts. As displayed in Fig. 4f, when injecting 3 M methanol into the electrolyte, the relative current of Pt/C dropped sharply and was unable to recover. Unlike Pt/C, the current of Fe-N-GDCA_{0.8} showed a negligible raise because the additional methanol can dissolve more oxygen than pure 0.1 M KOH, further evidencing its brilliant stability and durability. Moreover, to highlight the excellence of GDCA_{0.8} matrix, commercial Acetylene carbon black and Ketjenblack (denoted as Fe-N-ACET and Fe-N-KJB) were used to compare (Fig. S23), Fe-N-GDCA_{0.8} also exhibited an active $E_{1/2}$ of 0.93 V than Fe-N-ACET (0.81 V) and Fe-N-KJB (0.87 V).

3.3. Aqueous zinc-air battery and quasi-solid zinc-air battery performance evaluation

To appraise the performance of the Fe-N-GDCA_{0.8} electrocatalyst in actual energy storage and conversion devices, we installed a primary aqueous Zinc-air battery (ZAB) by using 6 M KOH mixed with 0.2 M Zn (Ac)₂ as electrolyte. In order to evaluate the output work capability of the installation, universal meter and i-t technology were introduced to measure the open circuit voltage (OCV) of the catalysts. As depicted in Fig. 5a, the Fe-N-GDCA_{0.8} showed a higher OCV of 1.51 V, which was close to the theory value of 1.65 V. When it comes to Pt/C, the OCV only possessed 1.46 V (Fig. S24). This preliminarily illustrated that Fe-N-GDCA_{0.8} has a greater tendency to do external work. Meanwhile, specific capacity was also carried out to estimate the service durability of ZABs. As seen in Fig. 5b, the ZAB using Fe-N-GDCA_{0.8} as air electrode had an ultra-high specific capacity of 803.4 mAh g_{Zn}⁻¹ at 20 mA cm⁻², which was higher than the data of commercial Pt/C (758.6 mAh g_{Zn}⁻¹) and closed to the theoretical value of 824 mAh g_{Zn}⁻¹ [88]. The key parameter specific energy density was also calculated, the value of Fe-N-GDCA_{0.8} was as large as 981.6 Wh kg_{Zn}⁻¹, exceeding the 904.2 Wh kg_{Zn}⁻¹ of Pt/C (Fig. S25). Compared the peak power density of Fe-N-GDCA_{0.8} and Pt/C in Fig. 5c, the former exhibited a maximum power density of 234.9 mW cm⁻², the latter solely reached 177.1 mW cm⁻², which further proved the excellent performance of Fe-N-GDCA_{0.8} electrocatalyst (Table S4). In addition, to explore the stability of the Fe-N-GDCA_{0.8} when serving in assembled ZABs. The rate performance was compared with commercial Pt/C (Fig. 5d), Fe-N-GDCA_{0.8} whether

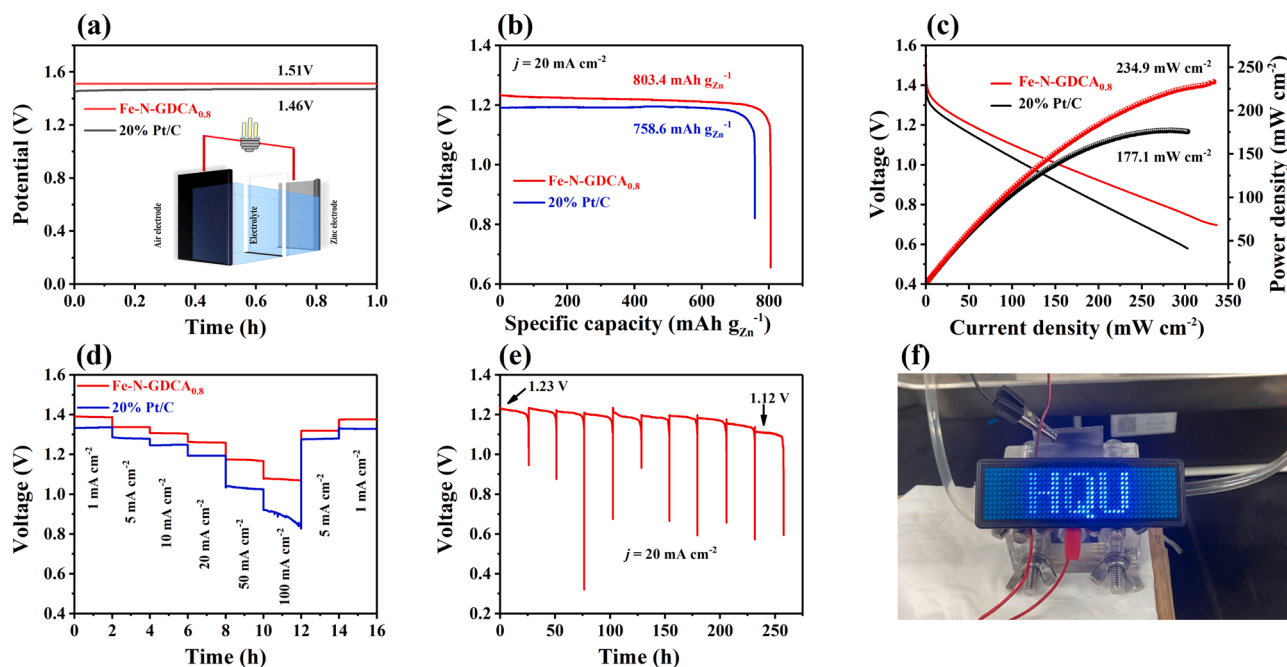


Fig. 5. Electrochemical performance of aqueous ZABs. (a) Open circuit potential of Fe-N-GDCA_{0.8} and Pt/C (inset: plot of aqueous ZABs). (b) Galvanostatic discharge curves of the aqueous ZABs at a current density of 20 mA cm^{-2} . The specific capacitance was calculated based on the mass loss of consumed Zn. (c) Discharge polarization curves and the corresponding power density curves of the aqueous ZABs using Fe-N-GDCA_{0.8} and Pt/C as air electrodes respectively. (d) The galvanostatic discharge curves of the aqueous ZABs at various current densities using Fe-N-GDCA_{0.8} and Pt/C as air electrodes respectively. (e) Long-term discharge curve with Fe-N-GDCA_{0.8} as an air electrode. (f) The digital photograph of the LED screen powered by liquid ZABs using Fe-N-GDCA_{0.8} as the ORR catalyst.

at low current density or high current density both showed excellent stability while Pt/C started to attenuate at 100 mA cm^{-2} . Meanwhile, we adopted the method of replacing the zinc plate and electrolyte whenever the ZAB completed the process of discharge. As depicted in

Fig. 5e, our electrocatalyst applied in ZABs showed little voltage drop after 260 h discharge at a current density of 20 mA cm^{-2} , exhibiting superior durability of Fe-N-GDCA_{0.8}. Moreover, the ZAB was also applied in the practical device and can support screen lighting

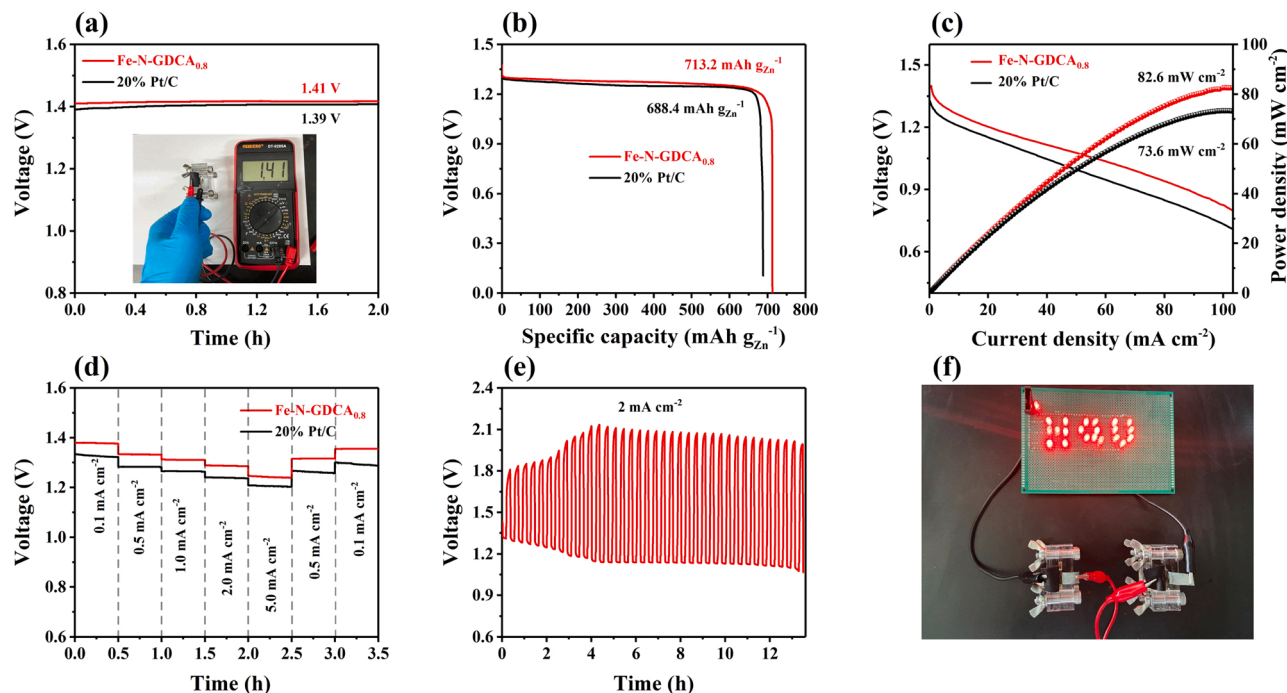


Fig. 6. Electrochemical performance of quasi-solid ZABs. (a) Open circuit potential of Fe-N-GDCA_{0.8} and Pt/C. (b) Galvanostatic discharge curves of the quasi solid ZABs at a current density of 2 mA cm^{-2} . The specific capacitance was calculated based on the mass loss of consumed Zn. (c) Discharge polarization curves and the corresponding power density curves of the quasi-solid ZABs using Fe-N-GDCA_{0.8} and Pt/C as air electrodes respectively. (d) The galvanostatic discharge curves of the quasi- solid ZABs at various current densities using Fe-N-GDCA_{0.8} and Pt/C as air electrodes respectively. (e) Charge and discharge curve with Fe-N-GDCA_{0.8} as an air electrode. (f) The digital photograph of the light emitting diode lightened by quasi-solid ZABs using Fe-N-GDCA_{0.8} as the ORR catalyst.

(Fig. 5f), highlighting its potential application value in portable electronic devices.

To avoid the hazard of liquid leakage in aqueous ZABs and respond to the requirements of small wearable devices in the rapid development of society, solid-state zinc-air batteries (SZABs) were created to solve the problems [89–92]. Taking this into consideration, we also constructed a solid-state ZAB with Fe-N-GDCA_{0.8} as cathode catalyst. As shown in Fig. 6a, c, the solid-state ZAB exhibited a maximum power density of 82.6 mW cm⁻² and an open circuit potential of 1.41 V, which outperformed most SZABs previously reported. When we executed a current density of 2 mA cm⁻², Fe-N-GDCA_{0.8} possessed a longer discharge time than Pt/C (Fig. S26). Converting the discharge time to specific capacity by dividing the consumed mass of zinc, Fe-N-GDCA_{0.8} based quasi-solid ZAB achieved a high specific capacity of 713.2 mAh g_{Zn}⁻¹, which was higher than 688.4 mAh g_{Zn}⁻¹ of Pt/C (Fig. 6b). In order to emphasize the advantage of Fe-N-GDCA_{0.8}, the previously published works of literature were also used to compare (Table S5). Discharge curves at different current densities were compared to evaluate the rate performance of the catalyst. Fe-N-GDCA_{0.8} showed relatively stable curves whether low or high current, especially after high current it can also recover a steady current platform (Fig. 6d). The charge/discharge property of quasi-solid ZAB equipping Fe-N-GDCA_{0.8} was also stable during 13 h cycling (Fig. 6e). Further confirming the excellent durability of Fe-N-GDCA_{0.8}. Quasi-solid ZABs in series can light up considerable homemade light-emitting diode (LED, Fig. 6f), evidencing its practicability in micro-type light-emitting devices.

4. Conclusion

In summary, by synthesizing self-doping heteroatoms and porous GDCA as carbon supports to accommodation and isolation of Fe(II)-phenanthroline precursors and subsequent pyrolysis, a series of Fe-N-GDCA_x for efficient ORR have been successfully fabricated. Taking the advantage of the excellent hierarchical porosity and abundant self-doping heteroatoms, the Fe-N₄ active sites can uniformly form and sufficiently expose on the GDCA_{0.8}. In addition, compared with the previously reported superior E_{1/2}, Fe-N-GDCA_{0.8} do not need other assisted gas like NH₃ and H₂, it can reach the outstanding half-wave potential of 0.93 V, outperforming the commercially available Pt/C and a great deal of published precious-free metal catalysts. The practical energy storage and conversion devices like ZABs and quasi-solid ZABs both got an exceedingly good performance by using Fe-N-GDCA_{0.8} as air cathode. Aqueous primary ZAB achieved a superb specific capacity of 803.4 mAh g_{Zn}⁻¹ and a high peak power density of 234 mW cm⁻² as well as kept stability after 260 h working. Quasi-solid ZAB also exhibited a wonderful specific capacity of 713.2 mAh g_{Zn}⁻¹, delivering a remarkable maximum power density of 82.6 mW cm⁻² and an excellent rate performance. We believe this study would give an inspiration for constructing multi-level cross-linked coupling carbon support and SACs to apply in other catalytic fields such as CO₂ reduction reaction and N₂ reduction reaction.

CRediT authorship contribution statement

Tao Wu: Writing – original draft, Methodology, Formal analysis. **Shufei Zhu:** Data curation, Investigation. **Qian Ma:** Supervision, Validation. **Yiming Xie:** Writing – review & editing. **Canzhong Lu:** Funding acquisition, Conceptualization.

Declaration of Competing Interest

The authors declare that they have no known competing financial interests or personal relationships that could have appeared to influence the work reported in this paper.

Data Availability

Data will be made available on request.

Acknowledgements

This work was supported by the National Natural Science Foundation of China and the authors sincerely thank the National Natural Science Foundation of China (22271106 and 21875252). The authors would like to thank Instrumental Analysis Center of Huaqiao University for Raman spectrum test. The authors would like to thank Miss Chen Jing Ling at Instrumental Analysis Center of Huaqiao University for their assistance with Raman analysis. The authors would like to thank Gu Yun from Shiyanjia Lab (www.shiyanjia.com) for the XPS and HAADF-STEM test.

Appendix A. Supporting information

Supplementary data associated with this article can be found in the online version at [doi:10.1016/j.apcatb.2023.122685](https://doi.org/10.1016/j.apcatb.2023.122685).

References

- [1] J. Fu, R. Liang, G. Liu, A. Yu, Z. Bai, L. Yang, Z. Chen, Recent progress in electrically rechargeable Zinc-air batteries, *Adv. Mater.* 31 (2019) 1805230, <https://doi.org/10.1002/adma.201805230>.
- [2] Y. Li, H. Dai, Recent advances in Zinc-air batteries, *Chem. Soc. Rev.* 43 (2014) 5257–5275, <https://doi.org/10.1039/c4cs00015c>.
- [3] H.-F. Wang, C. Tang, Q. Zhang, A review of precious-metal-free bifunctional oxygen electrocatalysts: rational design and applications in Zn-air batteries, *Adv. Funct. Mater.* 28 (2018) 1803329, <https://doi.org/10.1002/adfm.201803329>.
- [4] J. Yi, P. Liang, X. Liu, K. Wu, Y. Liu, Y. Wang, Y. Xia, J. Zhang, Challenges, mitigation strategies and perspectives in development of Zinc-electrode materials and fabrication for rechargeable Zinc-air batteries, *Energy Environ. Sci.* 11 (2018) 3075–3095, <https://doi.org/10.1039/c8ee01991f>.
- [5] H. Liu, F. Yu, K. Wu, G. Xu, C. Wu, H.-K. Liu, S.-X. Dou, Recent progress on Fe-based single/dual-atom catalysts for Zn-Air batteries, *Small* 18 (2022) 2106635, <https://doi.org/10.1002/sml.202106635>.
- [6] Y. Zheng, W. Xiao, M. Cho, K. Cho, Density functional theory calculations for the oxygen dissociation on nitrogen and transition metal doped graphenes, *Chem. Phys. Lett.* 586 (2013) 104–107, <https://doi.org/10.1016/j.cplett.2013.09.016>.
- [7] S. Kattel, G. Wang, Reaction pathway for oxygen reduction on FeN₄ embedded graphene, *J. Phys. Chem. Lett.* 5 (2014) 452–456, <https://doi.org/10.1021/jz402717r>.
- [8] X. Wan, X. Liu, Y. Li, R. Yu, L. Zheng, W. Yan, H. Wang, M. Xu, J. Shui, Fe-N-C electrocatalyst with dense active sites and efficient mass transport for high-performance proton exchange membrane fuel cells, *Nat. Catal.* 2 (2019) 259–268, <https://doi.org/10.1038/s41929-019-0237-3>.
- [9] D. Menga, J.-L. Low, Y.-S. Li, I. Arcon, B. Koyuturk, F. Wagner, F. Ruiz-Zepeda, M. Gaberscek, B. Paulus, T.-P. Feller, Resolving the dilemma of Fe-N-C catalysts by the selective synthesis of tetrapyrrolic active sites via an imprinting strategy, *J. Am. Chem. Soc.* 143 (2021) 18010–18019, <https://doi.org/10.1021/jacs.1c04884>.
- [10] X. Qu, Y. Han, Y. Chen, J. Lin, G. Li, J. Yang, Y. Jiang, S. Sun, Stepwise pyrolysis treatment as an efficient strategy to enhance the stability performance of Fe-N_x/C electrocatalyst towards oxygen reduction reaction and proton exchange membrane fuel cell, *Appl. Catal. B: Environ.* 295 (2021), 120311, <https://doi.org/10.1016/j.apcatb.2021.120311>.
- [11] L. Hu, C. Dai, L. Chen, Y. Zhu, Y. Hao, Q. Zhang, L. Gu, X. Feng, S. Yuan, L. Wang, B. Wang, Metal-triazolate-framework-derived FeN₄Cl₁ single-atom catalysts with hierarchical porosity for the oxygen reduction reaction, *Angew. Chem. Int. Ed.* 60 (2021) 27324–27329, <https://doi.org/10.1002/anie.202113895>.
- [12] Q. Wang, L. Shang, D. Sun-Waterhouse, T. Zhang, G. Waterhouse, Engineering local coordination environments and site densities for high-performance Fe-N-C oxygen reduction reaction electrocatalysis, *SmartMat* 2 (2021) 154–175, <https://doi.org/10.1002/smm2.1033>.
- [13] Y. Wang, J. Mao, X. Meng, L. Yu, D. Deng, X. Bao, Catalysis with two-dimensional materials confining single atoms: concept, design, and applications, *Chem. Rev.* 119 (2019) 1806–1854, <https://doi.org/10.1021/acs.chemrev.8b00501>.
- [14] C.-X. Zhao, B.-Q. Li, J.-N. Liu, Q. Zhang, Intrinsic electrocatalytic activity regulation of M-N-C single-atom catalysts for the oxygen reduction reaction, *Angew. Chem. Int. Ed.* 60 (2021) 4448–4463, <https://doi.org/10.1002/anie.202003917>.
- [15] J. Yang, W. Li, D. Wang, Y. Li, Single-atom materials: small structures determine macroproperties, *Small Struct.* 2 (2020) 2000051, <https://doi.org/10.1002/sstr.202000051>.
- [16] A. Mehmood, M. Gong, F. Jaouen, A. Roy, A. Zitolo, A. Khan, M.-T. Sougrati, M. Primbs, A.M. Bonastre, D. Fongalland, G. Drazic, P. Strasser, A. Kucernak, High loading of single atomic iron sites in Fe-NC oxygen reduction catalysts for proton

- exchange membrane fuel cells, *Nat. Catal.* 5 (2022) 311–323, <https://doi.org/10.1038/s41929-022-00772-9>.
- [17] L.-S. Zhang, X.-H. Jiang, Z.-A. Zhong, L. Tian, Q. Sun, Y.-T. Cui, X. Lu, J.-P. Zou, S.-L. Luo, Carbon nitride supported high-loading Fe single-atom catalyst for activation of peroxydisulfate to generate $^1\text{O}_2$ with 100% selectivity, *Angew. Chem. Int. Ed.* 60 (2021) 21751–21755, <https://doi.org/10.1002/anie.202109488>.
 - [18] G. Chen, Y. An, S. Liu, F. Sun, H. Qi, H. Wu, Y. He, P. Liu, R. Shi, J. Zhang, A. Kuc, U. Kaiser, T. Zhang, T. Heine, G. Wu, X. Feng, Highly accessible and dense surface single metal FeN₄ active sites for promoting the oxygen reduction reaction, *Energy Environ. Sci.* 15 (2022) 2619–2628, <https://doi.org/10.1039/d2ee00542e>.
 - [19] M. Zhao, H. Liu, H. Zhang, W. Chen, H. Sun, Z. Wang, B. Zhang, L. Song, Y. Yang, C. Ma, Y. Han, W. Huang, A pH-universal ORR catalyst with single-atom iron sites derived from a double-layer MOF for superior flexible quasi-solid-state rechargeable Zn–air batteries, *Energy Environ. Sci.* 14 (2021) 6455–6463, <https://doi.org/10.1039/d1ee01602d>.
 - [20] X. Xie, L. Peng, H. Yang, G.I.N. Waterhouse, L. Shang, T. Zhang, MIL-101-derived mesoporous carbon supporting highly exposed Fe single-atom sites as efficient oxygen reduction reaction catalysts, *Adv. Mater.* 33 (2021) 2101038, <https://doi.org/10.1002/adma.202101038>.
 - [21] W. Wang, Y. Wu, T. Liu, Y. Zhao, Y. Qu, R. Yang, Z. Xue, Z. Wang, F. Zhou, J. Long, Z. Yang, X. Han, Y. Lin, M. Chen, L. Zheng, H. Zhou, X. Lin, F. Wu, H. Wang, Y. Yang, Y. Li, Y. Dai, Y. Wu, Single Co sites in ordered SiO₂ channels for boosting nonoxidative propane dehydrogenation, *ACS Catal.* 12 (2022) 2632–2638, <https://doi.org/10.1021/acscatal.1c05921>.
 - [22] K. Ai, Y. Liu, C. Ruan, L. Lu, G. Lu, Sp² C-dominant N-doped carbon sub-micrometer spheres with a tunable size: a versatile platform for highly efficient oxygen-reduction catalysts, *Adv. Mater.* 25 (2013) 998–1003, <https://doi.org/10.1002/adma.201203923>.
 - [23] L. Shang, H. Yu, X. Huang, T. Bian, R. Shi, Y. Zhao, G.I.N. Waterhouse, L.-Z. Wu, C.-H. Tung, T. Zhang, Well-dispersed ZIF-derived Co,N-Co-doped carbon nanoframes through mesoporous-silica-protected calcination as efficient oxygen reduction electrocatalysts, *Adv. Mater.* 28 (2016) 1668–1674, <https://doi.org/10.1002/adma.201505045>.
 - [24] X. Fu, G. Jiang, G. Wen, R. Gao, S. Li, M. Li, J. Zhu, Y. Zheng, Z. Li, Y. Hu, L. Yang, Z. Bai, A. Yu, Z. Chen, Densely accessible Fe-N_x active sites decorated mesoporous carbon-spheres for oxygen reduction towards high performance aluminum-air flow batteries, *Appl. Catal. B: Environ.* 293 (2021), 120176, <https://doi.org/10.1016/j.apcatb.2021.120176>.
 - [25] X. Zhang, S. Zhang, Y. Yang, L. Wang, Z. Mu, H. Zhu, X. Zhu, H. Xing, H. Xia, B. Huang, J. Li, S. Guo, E. Wang, A general method for transition metal single atoms anchored on honeycomb-like nitrogen-doped carbon nanosheets, *Adv. Mater.* 32 (2020) 1906905, <https://doi.org/10.1002/adma.201906905>.
 - [26] Q. Wang, Y. Yang, F. Sun, G. Chen, J. Wang, L. Peng, W.T. Chen, L. Shang, J. Zhao, D. Sun-Waterhouse, T. Zhang, G.I.N. Waterhouse, Molten NaCl-assisted synthesis of porous Fe-N-C electrocatalysts with a high density of catalytically accessible FeN₄ active sites and outstanding oxygen reduction reaction performance, *Adv. Energy Mater.* 11 (2021) 2100219, <https://doi.org/10.1002/aenm.202100219>.
 - [27] H. Xu, D. Wang, P. Yang, L. Du, X. Lu, R. Li, L. Liu, J. Zhang, M. An, A hierarchically porous Fe-N-C synthesized by dual melt-salt-mediated template as advanced electrocatalyst for efficient oxygen reduction in Zinc-air battery, *Appl. Catal. B: Environ.* 305 (2022), 121040, <https://doi.org/10.1016/j.apcatb.2021.121040>.
 - [28] Y. Li, P. Zhang, L. Wan, Y. Zheng, X. Qu, H. Zhang, Y. Wang, K. Zaghbi, J. Yuan, S. Sun, Y. Wang, Z. Zhou, S. Sun, A general carboxylate-assisted approach to boost the ORR performance of ZIF-derived Fe/N/C catalysts for proton exchange membrane fuel cells, *Adv. Funct. Mater.* 31 (2021) 2009645, <https://doi.org/10.1002/adfm.202009645>.
 - [29] H. Yang, Z. Li, S. Kou, G. Lu, Z. Liu, A complex-sequestered strategy to fabricate Fe single-atom catalyst for efficient oxygen reduction in a broad pH-range, *Appl. Catal. B: Environ.* 278 (2020), 119270, <https://doi.org/10.1016/j.apcatb.2020.119270>.
 - [30] G. Chen, P. Liu, Z. Liao, F. Sun, Y. He, H. Zhong, T. Zhang, E. Zschech, M. Chen, G. Wu, J. Zhang, X. Feng, Zinc-mediated template synthesis of Fe-N-C electrocatalysts with densely accessible Fe-N_x active sites for efficient oxygen reduction, *Adv. Mater.* 32 (2020) 1907399, <https://doi.org/10.1002/adma.201907399>.
 - [31] M. Zhu, C. Zhao, X. Liu, X. Wang, F. Zhou, J. Wang, Y. Hu, Y. Zhao, T. Yao, L.-M. Yang, Y. Wu, Single atomic cerium sites with a high coordination number for efficient oxygen reduction in proton-exchange membrane fuel cells, *ACS Catal.* 11 (2021) 3923–3929, <https://doi.org/10.1021/acscatal.0c05503>.
 - [32] J. Li, N. Wang, J. Tian, W. Qian, W. Chu, Cross-coupled macro-mesoporous carbon network toward record high energy-power density supercapacitor at 4 V, *Adv. Funct. Mater.* 28 (2018) 1806153, <https://doi.org/10.1002/adfm.201806153>.
 - [33] Y. Chen, S. Hu, F. Nichols, F. Bridges, S. Kan, T. He, Y. Zhang, S. Chen, Carbon aerogels with atomic dispersion of binary iron–cobalt sites as effective oxygen catalysts for flexible Zinc–air batteries, *J. Mater. Chem. A* 8 (2020) 11649–11655, <https://doi.org/10.1039/d0ta04633g>.
 - [34] H. Yang, S. Kou, Z. Li, Z. Chang, M. Wang, Z. Liu, G. Lu, 3D interconnected nitrogen-self-doped carbon aerogels as efficient oxygen reduction electrocatalysts derived from biomass gelatin, *RSC Adv.* 9 (2019) 40301–40308, <https://doi.org/10.1039/c9ra07926b>.
 - [35] Z. Yang, X. Duan, J. Wang, Y. Li, X. Fan, F. Zhang, G. Zhang, W. Peng, Facile synthesis of high-performance nitrogen-doped hierarchically porous carbon for catalytic oxidation, *ACS Sustain. Chem. Eng.* 8 (2020) 4236–4243, <https://doi.org/10.1021/acssuschemeng.9b07469>.
 - [36] M. Liu, N. Li, S. Cao, X. Wang, X. Lu, L. Kong, Y. Xu, X.-H. Bu, A "pre-constrained metal twins" strategy to prepare efficient dual-metal-atom catalysts for cooperative oxygen electrocatalysis, *Adv. Mater.* 34 (2022) 2107421, <https://doi.org/10.1002/adma.202107421>.
 - [37] K. Khan, T. Liu, M. Arif, X. Yan, M.D. Hossain, F. Rehman, S. Zhou, J. Yang, C. Sun, S.H. Bae, J. Kim, K. Amine, X. Pan, Z. Luo, Laser-irradiated holey graphene-supported single-atom catalyst towards hydrogen evolution and oxygen reduction, *Adv. Energy Mater.* 11 (2021) 2101619, <https://doi.org/10.1002/aenm.202101619>.
 - [38] J. Xie, B.-Q. Li, H.-J. Peng, Y.-W. Song, J.-X. Li, Z.-W. Zhang, Q. Zhang, From supramolecular species to self-templated porous carbon and metal-doped carbon for oxygen reduction reaction catalysts, *Angew. Chem. Int. Ed.* 58 (2019) 4963–4967, <https://doi.org/10.1002/anie.201814605>.
 - [39] C. Du, Y. Gao, J. Wang, W. Chen, A new strategy for engineering a hierarchical porous carbon-anchored Fe single-atom electrocatalyst and the insights into its bifunctional catalysis for flexible rechargeable Zn–air batteries, *J. Mater. Chem. A* 8 (2020) 9981–9990, <https://doi.org/10.1039/d0ta03457f>.
 - [40] J. Cao, C. Zhu, Y. Aoki, H. Habazaki, Starch-derived hierarchical porous carbon with controlled porosity for high performance supercapacitors, *ACS Sustain. Chem. Eng.* 6 (2018) 7292–7303, <https://doi.org/10.1021/acssuschemeng.7b04459>.
 - [41] C. Wang, D. Wu, H. Wang, Z. Gao, F. Xu, K. Jiang, A green and scalable route to yield porous carbon sheets from biomass for supercapacitors with high capacity, *J. Mater. Chem. A* 6 (2018) 1244–1254, <https://doi.org/10.1039/c7ta07579k>.
 - [42] X. Wan, X. Liu, Y. Li, R. Yu, L. Zheng, W. Yan, H. Wang, M. Xu, J. Shui, Fe-N-C electrocatalyst with dense active sites and efficient mass transport for high-performance proton exchange membrane fuel cells, *Nat. Catal.* 2 (2019) 259–268, <https://doi.org/10.1038/s41929-019-0237-3>.
 - [43] W.Y. Noh, J. Mun, Y. Lee, E.M. Kim, Y.K. Kim, K.Y. Kim, H.Y. Jeong, J.H. Lee, H.-K. Song, G. Lee, J.S. Lee, Molecularly engineered carbon platform to anchor edge-hosted single-atomic M-N/C (M = Fe, Co, Ni, Cu) electrocatalysts of outstanding durability, *ACS Catal.* 12 (2022) 7994–8006, <https://doi.org/10.1021/acscatal.2c00697>.
 - [44] H. Zhou, T. Yang, Z. Kou, L. Shen, Y. Zhao, Z. Wang, X. Wang, Z. Yang, J. Du, J. Xu, M. Chen, L. Tian, W. Guo, Q. Wang, H. Lv, W. Chen, X. Hong, J. Luo, D. He, Y. Wu, Negative pressure pyrolysis induced highly accessible single sites dispersed on 3D graphene frameworks for enhanced oxygen reduction, *Angew. Chem. Int. Ed.* 59 (2020) 20465–20469, <https://doi.org/10.1002/anie.202009700>.
 - [45] Y. Jiang, L. Yang, T. Sun, J. Zhao, Z. Lyu, O. Zhuo, X. Wang, Q. Wu, J. Ma, Z. Hu, Significant contribution of intrinsic carbon defects to oxygen reduction activity, *ACS Catal.* 5 (2015) 6707–6712, <https://doi.org/10.1021/acscatal.5b01835>.
 - [46] R. Jiang, L. Li, T. Sheng, G. Hu, Y. Chen, L. Wang, Edge-site engineering of atomically dispersed Fe-N₄ by selective C-N bond cleavage for enhanced oxygen reduction reaction activities, *J. Am. Chem. Soc.* 140 (2018) 11594–11598, <https://doi.org/10.1021/jacs.8b07294>.
 - [47] J. Wang, G. Han, L. Wang, L. Du, G. Chen, Y. Gao, Y. Ma, C. Du, X. Cheng, P. Zuo, G. Yin, ZIF-8 with ferrocene encapsulated: a promising precursor to single-atom Fe embedded nitrogen-doped carbon as highly efficient catalyst for oxygen electroreduction, *Small* 14 (2018) 1704282, <https://doi.org/10.1002/smll.201704282>.
 - [48] Y. Han, H. Duan, C. Zhou, H. Meng, Q. Jiang, B. Wang, W. Yan, R. Zhang, Stabilizing cobalt single atoms via flexible carbon membranes as bifunctional electrocatalysts for binder-free Zinc-air batteries, *Nano Lett.* 22 (2022) 2497–2505, <https://doi.org/10.1021/acs.nanolett.2c00278>.
 - [49] A. Han, W. Chen, S. Zhang, M. Zhang, Y. Han, J. Zhang, S. Ji, L. Zheng, Y. Wang, L. Gu, C. Chen, Q. Peng, D. Wang, Y. Li, A polymer encapsulation strategy to synthesize porous nitrogen-doped carbon-nanosphere-supported metal isolated-single-atomic-site catalysts, *Adv. Mater.* 30 (2018) 1706508, <https://doi.org/10.1002/adma.201706508>.
 - [50] S.-N. Zhao, J.-K. Li, R. Wang, J. Cai, S.-Q. Zang, Electronically and geometrically modified single-atom Fe sites by adjacent Fe nanoparticles for enhanced oxygen reduction, *Adv. Mater.* 34 (2022) 2107291, <https://doi.org/10.1002/adma.202107291>.
 - [51] Y. Chen, S. Ji, Y. Wang, J. Dong, W. Chen, Z. Li, R. Shen, L. Zheng, Z. Zhuang, D. Wang, Y. Li, Isolated single iron atoms anchored on N-doped porous carbon as an efficient electrocatalyst for the oxygen reduction reaction, *Angew. Chem. Int. Ed.* 56 (2017) 6937–6941, <https://doi.org/10.1002/anie.201702473>.
 - [52] Y. Zhou, X. Tao, G. Chen, R. Lu, D. Wang, M.-X. Chen, E. Jin, J. Yang, H.-W. Liang, Y. Zhao, X. Peng, A. Narita, K. Mullen, Multilayer stabilization for fabricating high-loading single-atom catalysts, *Nat. Commun.* 11 (2020) 5892, <https://doi.org/10.1038/s41467-020-19599-8>.
 - [53] H. Adabi, A. Shakouri, N. Ul Hassan, J.R. Varcoe, B. Zulevi, A. Serov, J. R. Regalbuto, W.E. Mustain, High-performing commercial Fe-N-C cathode electrocatalyst for anion-exchange membrane fuel cells, *Nat. Energy* 6 (2021) 834–843, <https://doi.org/10.1038/s41560-021-00878-7>.
 - [54] V. Jose, H. Hu, E. Edison, W.J. Manalastas, H. Ren, P. Kidkhunthod, S. Sreejith, A. Jayakumar, J.M.V. Nsanzimana, M. Srinivasan, J. Choi, J.-M. Lee, Modulation of single atomic Co and Fe sites on hollow carbon nanospheres as oxygen electrodes for rechargeable Zn-air batteries, *Small Methods* 5 (2021) 2000751, <https://doi.org/10.1002/smt.202000751>.
 - [55] J.-D. Yi, R. Xu, Q. Wu, T. Zhang, K.-T. Zang, J. Luo, Y.-L. Liang, Y.-B. Huang, R. Cao, Atomically dispersed iron-nitrogen active sites within porphyrinic triazine-based frameworks for oxygen reduction reaction in both alkaline and acidic media, *ACS Energy Lett.* 3 (2018) 883–889, <https://doi.org/10.1021/acsenenergyl.8b00245>.
 - [56] W. Wei, X. Shi, P. Gao, S. Wang, W. Hu, X. Zhao, Y. Ni, X. Xu, Y. Xu, W. Yan, H. Ji, M. Cao, Well-elaborated, mechanochemically synthesized Fe-TPPCZIF precursors

- (Fe-TPP = tetraphenylporphyrin iron) to atomically dispersed iron-nitrogen species for oxygen reduction reaction and Zn-air batteries, *Nano Energy* 52 (2018) 29–37, <https://doi.org/10.1016/j.nanoen.2018.07.033>.
- [57] D. Wang, H. Xu, P. Yang, L. Xiao, L. Du, X. Lu, R. Li, J. Zhang, M. An, A dual-template strategy to engineer hierarchically porous Fe-N-C electrocatalysts for the high-performance cathodes of Zn-air batteries, *J. Mater. Chem. A* 9 (2021) 9761–9770, <https://doi.org/10.1039/d1ta00585e>.
- [58] Z. Yang, Y. Wang, M. Zhu, Z. Li, W. Chen, W. Wei, T. Yuan, Y. Qu, Q. Xu, C. Zhao, X. Wang, P. Li, Y. Li, Y. Wu, Y. Li, Boosting oxygen reduction catalysis with Fe-N₄ sites decorated porous carbons toward fuel cells, *ACS Catal.* 9 (2019) 2158–2163, <https://doi.org/10.1021/acscatal.8b04381>.
- [59] L. Peng, J. Yang, Y. Yang, F. Qian, Q. Wang, D. Sun-Waterhouse, L. Shang, T. Zhang, G.I.N. Waterhouse, Mesopore-rich Fe-N-C catalyst with FeN₄-O-NC single-atom sites delivers remarkable oxygen reduction reaction performance in alkaline media, *Adv. Mater.* 34 (2022) 2202544, <https://doi.org/10.1002/adma.202202544>.
- [60] L. Jiao, J. Li, L.L. Richard, Q. Sun, T. Stracensky, E. Liu, M.T. Sougrati, Z. Zhao, F. Yang, S. Zhong, H. Xu, S. Mukerjee, Y. Huang, D.A. Cullen, J.H. Park, M. Ferrandon, D.J. Myers, F. Jaouen, Q. Jia, Chemical vapour deposition of Fe-N-C oxygen reduction catalysts with full utilization of dense Fe-N₄ sites, *Nat. Mater.* 20 (2021) 1385–1391, <https://doi.org/10.1038/s41563-021-01030-2>.
- [61] K. Zhang, Y. Zhang, Q. Zhang, Z. Liang, L. Gu, W. Guo, B. Zhu, S. Guo, R. Zou, Metal-organic framework-derived Fe/Cu-substituted Co nanoparticles embedded in CNTs-grafted carbon polyhedron for Zn-air batteries, *Carbon Energy* 2 (2020) 283–293, <https://doi.org/10.1002/cey2.35>.
- [62] S. Yi, X. Qin, C. Liang, J. Li, R. Rajagopalan, Z. Zhang, J. Song, Y. Tang, F. Cheng, H. Wang, M. Shao, Insights into KMnO₄ etched N-rich carbon nanotubes as advanced electrocatalysts for Zn-air batteries, *Appl. Catal. B: Environ.* 264 (2020), 118537, <https://doi.org/10.1016/j.apcatb.2019.118537>.
- [63] J. Han, X. Meng, L. Lu, J. Bian, Z. Li, C. Sun, Single-atom Fe-N_x-C as an efficient electrocatalyst for Zinc-air batteries, *Adv. Funct. Mater.* 29 (2019) 1808872, <https://doi.org/10.1002/adfm.201808872>.
- [64] J. Li, Y. Song, G. Zhang, H. Liu, Y. Wang, S. Sun, X. Guo, Pyrolysis of self-assembled iron porphyrin on carbon black as core/shell structured electrocatalysts for highly efficient oxygen reduction in both alkaline and acidic medium, *Adv. Funct. Mater.* 27 (2017) 1604356, <https://doi.org/10.1002/adfm.201604356>.
- [65] L. Tao, Q. Wang, S. Dou, Z. Ma, J. Huo, S. Wang, L. Dai, Edge-rich and dopant-free graphene as a highly efficient metal-free electrocatalyst for the oxygen reduction reaction, *Chem. Commun.* 52 (2016) 2764–2767, <https://doi.org/10.1039/c5cc09173j>.
- [66] C. Tang, Q. Zhang, Nanocarbon for oxygen reduction electrocatalysis: dopants, edges, and defects, *Adv. Mater.* 29 (2017) 1604103, <https://doi.org/10.1002/adma.201604103>.
- [67] Q. Li, H. Liu, L.-C. Zhang, H. Chen, H. Zhu, Y. Wu, M. Xu, S.-J. Bao, Highly efficient Fe-N-C oxygen reduction electrocatalyst engineered by sintering atmosphere, *J. Power Sources* 449 (2020), 227497, <https://doi.org/10.1016/j.jpowsour.2019.227497>.
- [68] Y. Jiang, Y.-P. Deng, R. Liang, N. Chen, G. King, A. Yu, Z. Chen, Linker-compensated metal-organic framework with electron delocalized metal sites for bifunctional oxygen electrocatalysis, *J. Am. Chem. Soc.* 144 (2022) 4783–4791, <https://doi.org/10.1021/jacs.1c10295>.
- [69] J. Qin, H. Liu, P. Zou, R. Zhang, C. Wang, H.L. Xin, Altering ligand fields in single-atom sites through second-shell anion modulation boosts the oxygen reduction reaction, *J. Am. Chem. Soc.* 144 (2022) 2197–2207, <https://doi.org/10.1021/jacs.1c11331>.
- [70] Y. Yan, S. Liang, X. Wang, M. Zhang, S.-M. Hao, X. Cui, Z. Li, Z. Lin, Robust wrinkled MoS₂/N-C bifunctional electrocatalysts interfaced with single Fe atoms for wearable Zinc-air batteries, *Proc. Natl. Acad. Sci. U.S.A.* 118 (2021) 2110036118, <https://doi.org/10.1073/pnas.2110036118>.
- [71] X. Ge, G. Su, W. Che, J. Yang, X. Zhou, Z. Wang, Y. Qu, T. Yao, W. Liu, Y. Wu, Atomic filtration by graphene oxide membranes to access atomically dispersed single atom catalysts, *ACS Catal.* 10 (2020) 10468–10475, <https://doi.org/10.1021/acscatal.0c02203>.
- [72] H. Fei, J. Dong, Y. Feng, C.S. Allen, C. Wan, B. Voloskiy, M. Li, Z. Zhao, Y. Wang, H. Sun, P. An, W. Chen, Z. Guo, C. Lee, D. Chen, I. Shakir, M. Liu, T. Hu, Y. Li, A. I. Kirkland, X. Duan, Y. Huang, General synthesis and definitive structural identification of MN₄C₄ single-atom catalysts with tunable electrocatalytic activities, *Nat. Catal.* 1 (2018) 63–72, <https://doi.org/10.1038/s41929-017-0008-y>.
- [73] S. Yang, X. Xue, X. Liu, W. Liu, J. Bao, Y. Huang, H. Su, S. Yuan, H. Li, Scalable synthesis of microporous iron-nitrogen-doped carbon as highly active and stable oxygen reduction electrocatalyst, *ACS Appl. Mater. Inter.* 11 (2019) 39263–39273, <https://doi.org/10.1021/acsami.9b10723>.
- [74] S. Wu, H. Liu, G. Lei, H. He, J. Wu, G. Zhang, F. Zhang, W. Peng, X. Fan, Y. Li, Single-atomic iron-nitrogen 2D MOF-originated hierarchically porous carbon catalysts for enhanced oxygen reduction reaction, *Chem. Eng. J.* 441 (2022), 135849, <https://doi.org/10.1016/j.cej.2022.135849>.
- [75] T. Chen, J. Wu, C. Zhu, Z. Liu, W. Zhou, C. Zhu, C. Guan, G. Fang, Rational design of iron single atom anchored on nitrogen doped carbon as a high-performance electrocatalyst for all-solid-state flexible Zinc-air batteries, *Chem. Eng. J.* 405 (2021), 125956, <https://doi.org/10.1016/j.cej.2020.125956>.
- [76] Y. Yuan, Q. Zhang, L. Yang, L. Wang, W. Shi, P. Liu, R. Gao, L. Zheng, Z. Chen, Z. Bai, Facet strain strategy of atomically dispersed Fe-N-C catalyst for efficient oxygen electrocatalysis, *Adv. Funct. Mater.* 32 (2022) 2206081, <https://doi.org/10.1002/adfm.202206081>.
- [77] X. Xie, L. Shang, X. Xiong, R. Shi, T. Zhang, Fe single-atom catalysts on MOF-5 derived carbon for efficient oxygen reduction reaction in proton exchange membrane fuel cells, *Adv. Energy Mater.* 12 (2021) 2102688, <https://doi.org/10.1002/aenm.202102688>.
- [78] F. Gui, Q. Jin, D. Xiao, X. Xu, Q. Tan, D. Yang, B. Li, P. Ming, C. Zhang, Z. Chen, S. Siahrostami, Q. Xiao, High-performance Zinc-air batteries based on bifunctional hierarchically porous nitrogen-doped carbon, *Small* 18 (2022) 2105928, <https://doi.org/10.1002/smll.202105928>.
- [79] L. Wan, W. Chen, H. Xu, Y. Wang, J. Yuan, Z. Zhou, S. Sun, A mild CO₂ etching method to tailor the pore structure of platinum-free oxygen reduction catalysts in proton exchange membrane fuel cells, *ACS Appl. Mater. Inter.* 13 (2021) 45661–45669, <https://doi.org/10.1021/acsaami.1c14709>.
- [80] V. Yarlagadda, M.K. Carpenter, T.E. Moylan, R.S. Kukreja, R. Koestner, W. Gu, L. Thompson, A. Kongkanand, Boosting fuel cell performance with accessible carbon mesopores, *ACS Energy Lett.* 3 (2018) 618–621, <https://doi.org/10.1021/acscenergylett.8b00186>.
- [81] A. Holewinski, S. Linic, Elementary mechanisms in electrocatalysis: revisiting the ORR Tafel slope, *J. Electrochem. Soc.* 159 (2012) H864–H870, <https://doi.org/10.1149/2.02221jes>.
- [82] G.-F. Wei, Y.-H. Fang, Z.-P. Liu, First principles Tafel kinetics for resolving key parameters in optimizing oxygen electrocatalytic reduction catalyst, *J. Phys. Chem. C* 116 (2012) 12696–12705, <https://doi.org/10.1021/jp3034616>.
- [83] L. Osmieri, A.H.A. Monteverde Videla, P. Ocón, S. Specchia, Kinetics of oxygen electroreduction on Me-N-C (Me = Fe, Co, Cu) catalysts in acidic medium: insights on the effect of the transition metal, *J. Phys. Chem. C* 121 (2017) 17796–17817, <https://doi.org/10.1021/acs.jpcc.7b02455>.
- [84] R. Zhou, Y. Zheng, M. Jaroniec, S.-Z. Qiao, Determination of the electron transfer number for the oxygen reduction reaction: from theory to experiment, *ACS Catal.* 6 (2016) 4720–4728, <https://doi.org/10.1021/acscatal.6b01581>.
- [85] G. Zhong, S. Xu, L. Liu, C.Z. Zheng, J. Dou, F. Wang, X. Fu, W. Liao, H. Wang, Effect of experimental operations on the limiting current density of oxygen reduction reaction evaluated by rotating-disk electrode, *ChemElectroChem* 7 (2020) 1107–1114, <https://doi.org/10.1002/celec.201902085>.
- [86] Y. Li, Y. Li, E. Zhu, T. McLouth, C.-Y. Chiu, C. Huang, Y. Huang, Stabilization of high-performance oxygen reduction reaction Pt electrocatalyst supported on reduced graphene oxide/carbon black composite, *J. Am. Chem. Soc.* 134 (2012) 12326–12329, <https://doi.org/10.1021/ja3031449>.
- [87] Y. Cheng, Y. Wang, Q. Wang, Z. Liao, N. Zhang, Y. Guo, Z. Xiang, Hierarchically porous metal-free carbon with record high mass activity for oxygen reduction and Zn-air batteries, *J. Mater. Chem. A* 7 (2019) 9831–9836, <https://doi.org/10.1039/c9ta02220a>.
- [88] R. Yuan, W. Bi, T. Zhou, N. Zhang, Ca Zhong, W. Chu, W. Yan, Q. Xu, C. Wu, Y. Xie, Two-dimensional hierarchical Fe-N-C electrocatalyst for Zn-Air batteries with ultrahigh specific capacity, *ACS Mater. Lett.* 2 (2019) 35–41, <https://doi.org/10.1021/acsmaterialslett.9b00386>.
- [89] P. Tan, B. Chen, H. Xu, H. Zhang, W. Cai, M. Ni, M. Liu, Z. Shao, Flexible Zn-and Li-air batteries: recent advances, challenges, and future perspectives, *Energy Environ. Sci.* 10 (2017) 2056–2080, <https://doi.org/10.1039/c7ee01913k>.
- [90] L. Yang, X. Zhang, L. Yu, J. Hou, Z. Zhou, R. Lv, Atomic Fe-N₄/C in flexible carbon fiber membrane as binder-free air cathode for Zn-Air batteries with stable cycling over 1000h, *Adv. Mater.* 34 (2022) 2105410, <https://doi.org/10.1002/adma.202105410>.
- [91] Z. Pei, Z. Yuan, C. Wang, S. Zhao, J. Fei, L. Wei, J. Chen, C. Wang, R. Qi, Z. Liu, Y. Chen, A flexible rechargeable Zinc-air battery with excellent low-temperature adaptability, *Angew. Chem. Int. Ed.* 59 (2020) 4793–4799, <https://doi.org/10.1002/anie.201915836>.
- [92] H. Liu, W. Xie, Z. Huang, C. Yao, Y. Han, W. Huang, Recent advances in flexible Zn-air batteries: materials for electrodes and electrolytes, *Small Methods* 6 (2022) 2101116, <https://doi.org/10.1002/smt.202101116>.